Pathogenic mutations in the chromokinesin KIF22 disrupt anaphase chromosome segregation

Alex F. Thompson[1], Patrick R. Blackburn[2,3], Noah S. Arons[1], Sarah N. Stevens[1], Dusica Babovic-Vuksanovic[2,4], Jane B. Lian[5], Eric W. Klee[6], Jason K. Stumpff[1*]

[1]Molecular Physiology and Biophysics, University of Vermont, Burlington, VT
[2]Laboratory Medicine and Pathology, Mayo Clinic, Rochester, MN
[3]Pathology, St. Jude Children's Research Hospital, Memphis, TN
[4]Clinical Genomics, Mayo Clinic, Rochester, MN
[5]Biochemistry, University of Vermont, Burlington, VT
[6]Biomedical Informatics, Mayo Clinic, Rochester, MN
*Corresponding author, jason.stumpff@uvm.edu

ABSTRACT

The chromokinesin KIF22 generates forces that contribute to mitotic chromosome congression and alignment. Mutations in the α2 helix of the motor domain of KIF22 have been identified in patients with abnormal skeletal development, and we report the identification of a patient with a novel mutation in the KIF22 tail. We demonstrate that pathogenic mutations do not result in a loss of KIF22's functions in early mitosis. Instead, mutations disrupt chromosome segregation in anaphase, resulting in reduced proliferation, abnormal daughter cell nuclear morphology, and, in a subset of cells, cytokinesis failure. This phenotype could be explained by a failure of KIF22 to inactivate in anaphase. Consistent with this model, constitutive activation of the motor via a known site of phosphoregulation in the tail phenocopied the effects of pathogenic mutations. These results suggest the motor domain α2 helix may be an important site for regulation of KIF22 activity at the metaphase to anaphase transition. In support of this conclusion, mimicking phosphorylation of α2 helix residue T158 also prevents inactivation of KIF22 in anaphase. These findings demonstrate the importance of both the head and tail of the motor in regulating the activity of KIF22 and offer insight into the cellular consequences of preventing KIF22 inactivation and disrupting force balance in anaphase.

INTRODUCTION

Mitosis requires mechanisms that mechanically control chromosome movements to ensure equal segregation of chromosomes to daughter cells. Forces that move mitotic chromosomes are generated by microtubule dynamics within the mitotic spindle and by molecular motor proteins. The chromokinesin KIF22 (or Kid, kinesin-like DNA-binding protein) is a plus-end directed member of the kinesin-10 family (Yajima et al., 2003). KIF22 and its orthologs, including

Nod (*Drosophila melanogaster*) (Zhang, Knowles, Goldstein, & Hawley, 1990) and Xkid (*Xenopus laevis*) (Antonio et al., 2000; Funabiki & Murray, 2000; Takagi, Itabashi, Suzuki, & Ishiwata, 2013), generate forces that move chromosomes away from the spindle poles. Structurally, KIF22 contains a conserved kinesin motor domain responsible for ATP hydrolysis and microtubule binding (Tokai et al., 1996; Yajima et al., 2003), a second microtubule binding domain in the tail (Shiroguchi, Ohsugi, Edamatsu, Yamamoto, & Toyoshima, 2003), a predicted coiled-coil domain (Shiroguchi et al., 2003), and a C-terminal DNA binding domain, which includes a helix-hairpin-helix motif (Tokai et al., 1996) **(Figure 1A)**. Precisely how KIF22's force generating activity is regulated in mitotic cells and how this regulation contributes to spindle function and cell viability remain incompletely understood.

In interphase, KIF22 localizes to the nucleus (Levesque & Compton, 2001; Tokai et al., 1996). As cells enter mitosis, chromosomes condense and KIF22 binds along chromosome arms (Levesque & Compton, 2001; Tokai et al., 1996). In prometaphase, chromosomes must congress and align at the center of the spindle. The interactions of the KIF22 motor domain with spindle microtubules and the KIF22 tail with chromosome arms allows the motor to generate polar ejection forces (Bieling, Kronja, & Surrey, 2010; Brouhard & Hunt, 2005), which push the arms of chromosomes away from the spindle poles and towards the center of the spindle (Marshall, Marko, Agard, & Sedat, 2001; Rieder & Salmon, 1994; Rieder, Davison, Jensen, Cassimeris, & Salmon, 1986), contributing to chromosome congression in prometaphase (Iemura & Tanaka, 2015; Levesque & Compton, 2001; Wandke et al., 2012), as well as chromosome arm orientation (Levesque & Compton, 2001; Wandke et al., 2012). In metaphase, polar ejection forces also contribute to chromosome oscillation and alignment (Antonio et al., 2000; Funabiki & Murray, 2000; Levesque & Compton, 2001; Levesque, Howard, Gordon, & Compton, 2003; Stumpff, Wagenbach, Franck, Asbury, & Wordeman, 2012; Takagi et al., 2013; Tokai-Nishizumi, Ohsugi, Suzuki, & Yamamoto, 2005). Purified KIF22 is monomeric (Shiroguchi et al., 2003; Yajima et al., 2003), and the forces generated by KIF22 on chromosomes arms may represent the collective action of many monomers. In anaphase, KIF22 is inactivated to reduce polar ejection forces and allow chromosomes to segregate towards the spindle poles (Soeda, Yamada-Nomoto, & Ohsugi, 2016; Su et al., 2016; Wolf, Wandke, Isenberg, & Geley, 2006)

The generation of polar ejection forces by KIF22 is regulated by the activity of cyclin-dependent kinase 1 (CDK1)/cyclin B, which is high in prometa- and metaphase, and drops sharply at the metaphase to anaphase transition when cyclin B is degraded (Hershko, 1999; Morgan, 1995). KIF22 is phosphorylated by CDK1/cyclin B at T463, a residue in the tail of the motor between the second microtubule binding and coiled-coil domains. Phosphorylation of T463 is

required for polar ejection force generation in prometa- and metaphase, and dephosphorylation of T463 is necessary for the suspension of polar ejection forces to allow chromosome segregation in anaphase (Soeda et al., 2016). Although a reduction of polar ejection forces in anaphase is a necessary step for proper anaphase chromosome segregation, it is not clear how this contributes to a shift in force balance within the spindle at the metaphase to anaphase transition. Furthermore, while several regions of the KIF22 tail are known to contribute to KIF22's inactivation as cells transition to anaphase, how motor activity is downregulated has not been resolved. Phosphoproteomic studies have identified sites of phosphorylation within KIF22's α2 helix (Kettenbach et al., 2011; Olsen et al., 2010; Rigbolt et al., 2011), suggesting this region, in addition to the tail, may also be important for the regulation of motor activity.

The study of pathogenic mutations can often provide insight into the regulation and function of cellular proteins. Mutations in KIF22 cause the developmental disorder spondyloepimetaphyseal dysplasia with joint laxity, leptodactylic type (SEMDJL2, also referred to as Hall Type or lepto-SEMDJL) (Boyden et al., 2011; Min et al., 2011; Tüysüz, Yılmaz, Erener-Ercan, Bilguvar, & Günel, 2014). Four point mutations in two amino acids have been reported in SEMDJL2 patients (Boyden et al., 2011; Min et al., 2011; Tüysüz et al., 2014) **(Figure 1A)**. These mutations occur in adjacent residues P148 and R149 in the α2 helix of the KIF22 motor domain **(Figure 1B)**. P148 and R149 are conserved in kinesin-10 family members across species **(Figure 1C)** and in many human members of the kinesin superfamily **(Figure 1D)**. However, no pathogenic mutations in the homologous proline or arginine residues have been recorded in OMIM (Online Mendelian Inheritance in Man, https://omim.org/). All identified patients are heterozygous for a single mutation in KIF22. Mutations in KIF22 dominantly cause SEMDJL2, and patients with both *de novo* and inherited mutations have been identified (Boyden et al., 2011; Min et al., 2011).

Although KIF22 mRNA is expressed throughout the body (Human Protein Atlas, http://www.proteinatlas.org (Uhlen et al., 2015)), the effects of these mutations are largely tissue-specific, and the development of the skeletal system is most affected in SEMDJL2 patients. A primary symptom of SEMDJL2 is short stature, resulting from shortening of both the trunk and the limbs. Additionally, patients presented with joint laxity, midface hypoplasia, scoliosis, and leptodactyly, a narrowing of the fingers (Boyden et al., 2011; Min et al., 2011). In very young children with SEMDJL2, the softness of the cartilage in the larynx and trachea caused respiratory issues (Boyden et al., 2011). Growth plate radiology demonstrated delayed maturation of the metaphyses and epiphyses in SEMDJL2 patients, and symptoms became more pronounced as

patients aged (Tüysüz et al., 2014). Leptodactyly, specifically, was only observed in older (young adult) patients (Boyden et al., 2011).

Pathogenic mutations in the KIF22 motor domain were predicted to be loss of function mutations (Min et al., 2011). However, KIF22 knockout in mice did not affect skeletal development. Loss of KIF22 was lethal early in embryogenesis for approximately 50% of embryos, but mice that survived past this point developed to adulthood and demonstrated no gross abnormalities or pathologies (Ohsugi et al., 2003). As such, the cellular mechanism by which mutations in KIF22 affect development is unknown.

Here we characterize an additional patient with a mutation in KIF22 and assess the effect of previously reported and novel pathogenic mutations on the function of KIF22 in mitosis. We demonstrate that mutations are not loss of function mutations, and do not alter the localization of the motor or the generation of polar ejection forces in prometaphase. Instead, mutations disrupt anaphase chromosome segregation, consistent with continued KIF22 activation and consequent polar ejection force generation in anaphase. Defects in anaphase chromosome segregation affect daughter cell nuclear morphology and, in a subset of cells, prevent cytokinesis. These findings demonstrate that anaphase inactivation of KIF22 is critical for daughter cell fitness. As such, mitotic defects may contribute to pathogenesis in patients with KIF22 mutations. Additionally, we demonstrate that aberrant polar ejection force generation in anaphase primarily affects the segregation of chromosomes by limiting chromosome arm movements in anaphase A and spindle pole separation in anaphase B, offering insight into the balance of forces required for accurate chromosome segregation in anaphase. Finally, we demonstrate that mimicking phosphorylation of T158 in the α2 helix disrupts anaphase chromosome segregation, confirming that the region of the motor domain affected by SEMDJL2 mutations also contributes to the mechanism by which KIF22 is inactivated in anaphase.

RESULTS

A novel mutation in KIF22 affects development

We report the identification and characterization of a patient with a novel mutation in KIF22 **(Figure 1E)**. The patient is a 15-year-old male with a history of short stature, cryptorchidism and shawl scrotum, minimal scoliosis, secondary enuresis, and skin hyperpigmentation. He presented for evaluation at 9 years of age. At that time, his height was just below 3% for age, weight was at 40% for age, and BMI was 82% for age. He was noted to have relative macrocephaly, with a head circumference at 93% for age. He had a broad forehead and hypertelorism, round face, flaring of eyebrows, and ankyloglossia. He also had mild brachydactyly **(Figure 1F)**. He had a history of

short stature since infancy, but followed a trajectory close to the third percentile. Growth hormone and thyroid function were normal. Bone age showed a normal, age-appropriate bone maturation with normal epiphyseal ossification centers. However, skeletal survey at age 11 years disclosed mild foreshortening of both 4th metacarpals **(Figure 1F)**, mild scoliosis of 14 degrees, as well as mild increase of the central anteroposterior diameter of several lower thoracic vertebrae with mild "bullet-shaped" appearance, and mild posterior scalloping of the lumbar vertebrae **(Figure 1G)**.

Genetic testing was performed to determine the cause of these developmental differences. Clinical whole exome sequencing revealed two variants of uncertain significance: a maternally inherited heterozygous *SLC26A2* variant [NM_000112.3(SLC26A2): c.1046T>A (p.F349Y)] (SCV000782516.1), as well as a *de novo* heterozygous *KIF22* variant [NM_007317.3(KIF22):c.1424T>G (p.V475G)] (SCV000782515.1) **(Figure 1E)**. The *SLC26A2* gene encodes the diastrophic dysplasia sulfate transporter (Haila et al., 2001; Rossi & Superti-Furga, 2001). However, results of carbohydrate deficient transferrin testing were not consistent with a congenital disorder of glycosylation (transferrin tri-sialo/di-oligo ratio 0.07).

The c.1424T>G, p.(V475G) *KIF22* variant has not been observed previously in the Genome Aggregation Database (gnomAD). This missense variant has mixed *in silico* predictions of significance **(Supplemental Table 1)**. According to American College of Medical Genetics 2015 criteria, the variant was classified as a variant of uncertain significance (VUS). V475 is located in the coiled-coil domain in the tail of KIF22 **(Figure 1A)**. This residue is conserved in most kinesin-10 family members across species **(Figure 1C)**. However, the tail domains of kinesin motors diverge in both structure and function, and as such meaningful alignments to assess the conservation of V475 across the human kinesin superfamily were not possible.

Figure 1

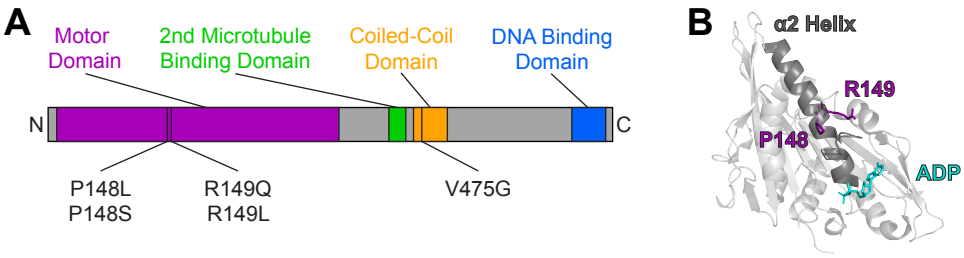

C

Homo sapiens	141	PEQPGVI**PR**ALMDLLQLTREE	161	468	RMVLMKT**V**EEKDLEI 482
Mus musculus	136	PEQPGVI**PR**ALMDLLQLAREE	156	463	RMVLMKT**V**EEKNLEI 477
Xenopus laevis	130	PNQPGVI**PR**AVRDLLQMSRTA	150	450	RMALLKK**W**EESQMEI 464
Danio rerio	117	QEQPGVI**PR**AVKEVFNLVGAQ	137	426	RLNLLKT**V**AQSRKEI 440
Bos taurus	136	PEQPGVI**PR**ALMDLLQLTREE	156	463	RMVLMKT**V**EEKDLEI 477
Drosophila melanogaster	107	PEHLGIL**PR**ALGDIFERVTAR	127	445	NSTLMGI**V**EETEPK- 459

D

KIF22	141	PEQPGVI**PR**ALMDLLQLTREE	161
KIF5A	122	PQLMGII**PR**IARDIFNHIYSM	142
KIF5B	121	PEGMGII**PR**IVQDIFNYIYSM	141
KIF5C	122	PQLMGII**PR**IAHDIFDHIYSM	142
KIF3A	116	PELRGII**P**NSFAHIFGHIAKA	136
KIF3B	112	PEKRGVI**P**NSFDHIFTHISRS	132
KIF3C	113	PELRGVI**P**NAFEHIFTHISRS	133
KIF17	107	PSQRGII**PR**AFEHVFESVQCA	127
KIF1A	112	KDQQGII**P**QLCEDLFSRINDT	132
KIF1B	112	ESQAGII**P**QLCEELFEKINDN	132
KIF1C	112	PGQQGIV**P**QLCEDLFSRVSEN	132
KIF13A	116	-EQLGLI**PR**LCCALFKRISLE	135
KIF13B	117	-DQPGLI**PR**LCSGLFERTQKE	136
KIF4B	108	EPTVGII**PR**VIQLLFKEIDKK	128
KIF7	114	EDEQGIV**PR**AMAEAFKLIDEN	135
KIF21A	108	EEELGII**SR**AVKHLFKSIEEK	128
KIF21B	107	EEEQGII**PR**AIAHLFGGIAER	127
KIF11	128	DPLAGII**PR**TLHQIFEKLTD-	147
KIF20A	176	--DGGIL**PR**SLALIFNSLQGQ	194
KIF20B	168	--NIGIL**PR**TLNVLFDSLQER	196
KIF23	128	--EGGLL**PR**CLDMIFNSIGSF	146
KIF10	101	--HLGVI**PR**AIHDIFQKIKKF	119
KIF18A	125	ADEPGVMYL**T**MLHLYKCMDEI	145
KIF18B	121	EGDPGIMYL**T**TVELYRRLEAR	141
KIF19	116	DQEPGIYVQ**T**LNDLFRAIEET	136
KIF6	113	YSDRGII**PR**TLSYIFEQLQKD	133
KIF9	109	YKHRGIL**PR**ALQQVFRMIEER	129
KIF12	128	PSLAGIM**QR**TFAWL---LDRV	145
KIF15	130	HNLRGVI**PR**SFEYLFSLIDRE	130

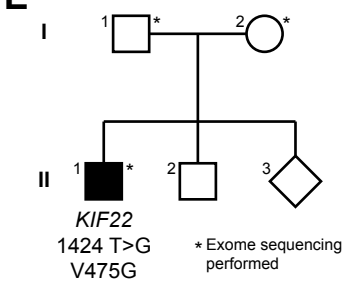

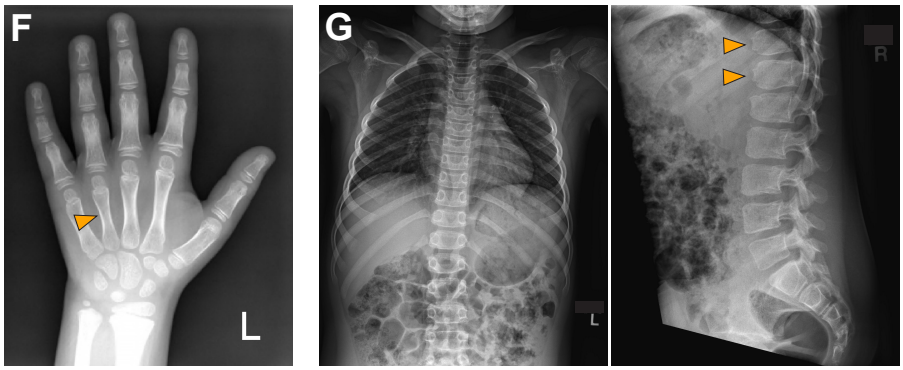

Figure 1. Identification of a novel pathogenic mutation in the tail of KIF22.

(A) Schematic of the domains of KIF22 with pathogenic mutations in the motor domain (magenta) and coiled-coil domain (yellow) indicated. **(B)** Location of amino acids P148 and R149 in the $\alpha 2$ helix of the KIF22 motor domain (PDB 6NJE). **(C)** Alignment of amino acid sequences of kinesin-10 family members to assess conservation of motor domain (P148 and R149, left) and coiled-coil domain (V475G, right) residues across species. **(D)** Alignment of amino acid sequences of human kinesin motors to assess conservation of motor domain residues across the kinesin superfamily. For C and D, alignments were performed using Clustal Omega. **(E)** Pedigree identifying the *de novo* V475G (1424 T>G) mutation. **(F)** Radiograph of the patient's hand, posteroanterior view. Arrowhead indicates mild foreshortening of the 4^{th} metacarpal. **(G)** Radiographs of the patient's spine. Left: anteroposterior view, right: lateral view. Arrowheads indicate "bullet-shaped" lower thoracic vertebrae.

Supplemental Table 1

Algorithm	Prediction
Sorting Intolerant from Tolerant (SIFT) (Vaser, Adusumalli, Leng, Sikic, & Ng, 2015)	Deleterious: score 0.01 with scores ranging from 0 to 1 and scores below 0.05 considered deleterious
Polymorphism Phenotyping (PolyPhen-2) (Adzhubei et al., 2010)	Benign: score 0.437
MutationTaster (Schwarz, Rödelsperger, Schuelke, & Seelow, 2010)	Deleterious
Combined Annotation Dependent Depletion (CADD) (Rentzsch, Witten, Cooper, Shendure, & Kircher, 2018)	Deleterious: scaled C-score 15.3800, with a score of greater than or equal to 10 indicating a deleterious substitution
Deleterious Annotation of Genetic Variants Using Neural Networks (DANN) (Quang, Chen, & Xie, 2015)	Deleterious: score 0.99 with scores ranging from 0 to 1 and higher values indicating a variant is more likely to be deleterious
Rare Exome Variant Ensemble Learner (REVEL) (Ioannidis et al., 2016)	Benign: score 0.28 with scores ranging from 0 to 1 and scores >0.803 classified as pathogenic

Pathogenic mutations in KIF22 do not disrupt the localization of the motor

To assess the effect of published pathogenic mutations in the motor domain and the novel pathogenic mutation in the tail on the function of KIF22 in mitosis, we generated human cervical adenocarcinoma (HeLa-Kyoto) cell lines with inducible expression of KIF22-GFP. Treatment of these cells with doxycycline induced KIF22-GFP expression at a level approximately two- to three-fold higher than the level of expression of endogenous KIF22 as measured by immunofluorescence **(Figure S1A-C)**. To facilitate both overexpression of and rescue with KIF22-GFP constructs, siRNA-resistant silent mutations were introduced into exogenous KIF22 **(Figure S1D-E)**. siRNA knockdown reduced levels of endogenous KIF22 by 87% (mean knockdown efficiency across HeLa-Kyoto cell lines) **(Figure S1D)**. Initial experiments were performed using HeLa-Kyoto cell lines expressing each known pathogenic mutation in KIF22 (P148L, P148S, R149L, R149Q, and V475G), and a subset of experiments then focused on cells expressing one representative motor domain mutation (R149Q) or the coiled-coil domain mutation in the tail (V475G). Additionally, we generated inducible retinal pigmented epithelial (RPE-1) cell lines expressing wild type and mutant KIF22-GFP to assess any differences between the consequences of expressing mutant KIF22 in aneuploid cancer-derived cells (HeLa-Kyoto) and genomically stable somatic cells. RPE-1 cells are human telomerase reverse transcriptase (hTERT)-immortalized (Bodnar et al., 1998), and metaphase chromosome spreads demonstrated that these cell lines are near-diploid, with a modal chromosome number of 46, even after selection to generate stable cell lines **(Figure S1F-G)**. The expression level of siRNA-resistant KIF22-GFP in RPE-1 cell lines was approximately four- to seven-fold higher than the level of expression of endogenous KIF22 **(Figure S1H-K)**, and siRNA knockdown reduced levels of endogenous KIF22 by 67% (mean knockdown efficiency across RPE-1 cell lines measured using immunofluorescence). As measurements of KIF22 depletion by immunofluorescence may include non-specific signal, this estimate of knockdown efficiency may underestimate the depletion of KIF22.

KIF22 localizes to the nucleus in interphase, and primarily localizes to chromosomes and spindle microtubules during mitosis (Tokai et al., 1996). KIF22-GFP with pathogenic mutations demonstrated the same localization pattern throughout the cell cycle as wild type motor (**Figure 2A)**. In all cell lines, KIF22-GFP was localized to the nucleus in interphase cells and was bound to condensing chromosomes in prophase. In prometaphase, metaphase, and anaphase mutant and wild type KIF22-GFP localized primarily to chromosome arms, with a smaller amount of motor signal visible on the spindle microtubules. The same localization patterns were seen for mutant and wild type KIF22-GFP expressed in RPE-1 cells **(Figure S2A)**.

Since mutations did not grossly disrupt localization of KIF22-GFP, fluorescence recovery after photobleaching (FRAP) was used to compare the dynamics of mutant and wild type KIF22 localization. In interphase nuclei, KIF22-GFP signal recovered completely 220 seconds after bleaching (97% ± 3% of intensity before bleaching, mean ± SEM), indicating a dynamic pool of KIF22-GFP **(Figure 2B and S2B)**. Similar high recovery percentages were also measured in interphase nuclei of cells expressing KIF22-GFP R149Q and KIF22-GFP V475G (100% ± 6% and 103% ± 7% at 220 seconds, respectively) **(Figure 2E and 2H)**. In contrast, KIF22-GFP recovery was minimal in cells bleached during metaphase and anaphase. Immediately after bleaching KIF22-GFP in metaphase cells, intensity was reduced to 18 ± 3% of initial intensity, and intensity had recovered to only 25% ± 3% after 220 seconds **(Figure 2C and S2B).** In anaphase, KIF22-GFP intensity immediately after bleaching was 17% ± 2% of initial intensity, and intensity recovered to 35% ± 6% of initial intensity after 220 seconds **(Figure 2D and S2B)**. This limited recovery indicates that KIF22 stably associates with mitotic chromosomes. Pathogenic mutations did not change these localization dynamics; recovery percentages in mitosis were also low in cells expressing KIF22-GFP R149Q (32 ± 3% of initial intensity in metaphase 220 seconds after bleaching, 39 ± 6% in anaphase) **(Figure 2F and 2G)** and KIF22-GFP V475G (29 ± 2% of initial intensity in metaphase, 35 ± 6% in anaphase) **(Figure 2I and 2J)**. These data indicate that pathogenic mutations do not alter the localization of KIF22 to chromosomes and spindle microtubules, and do not alter KIF22 localization dynamics in interphase, metaphase, or anaphase.

Supplemental Figure 1

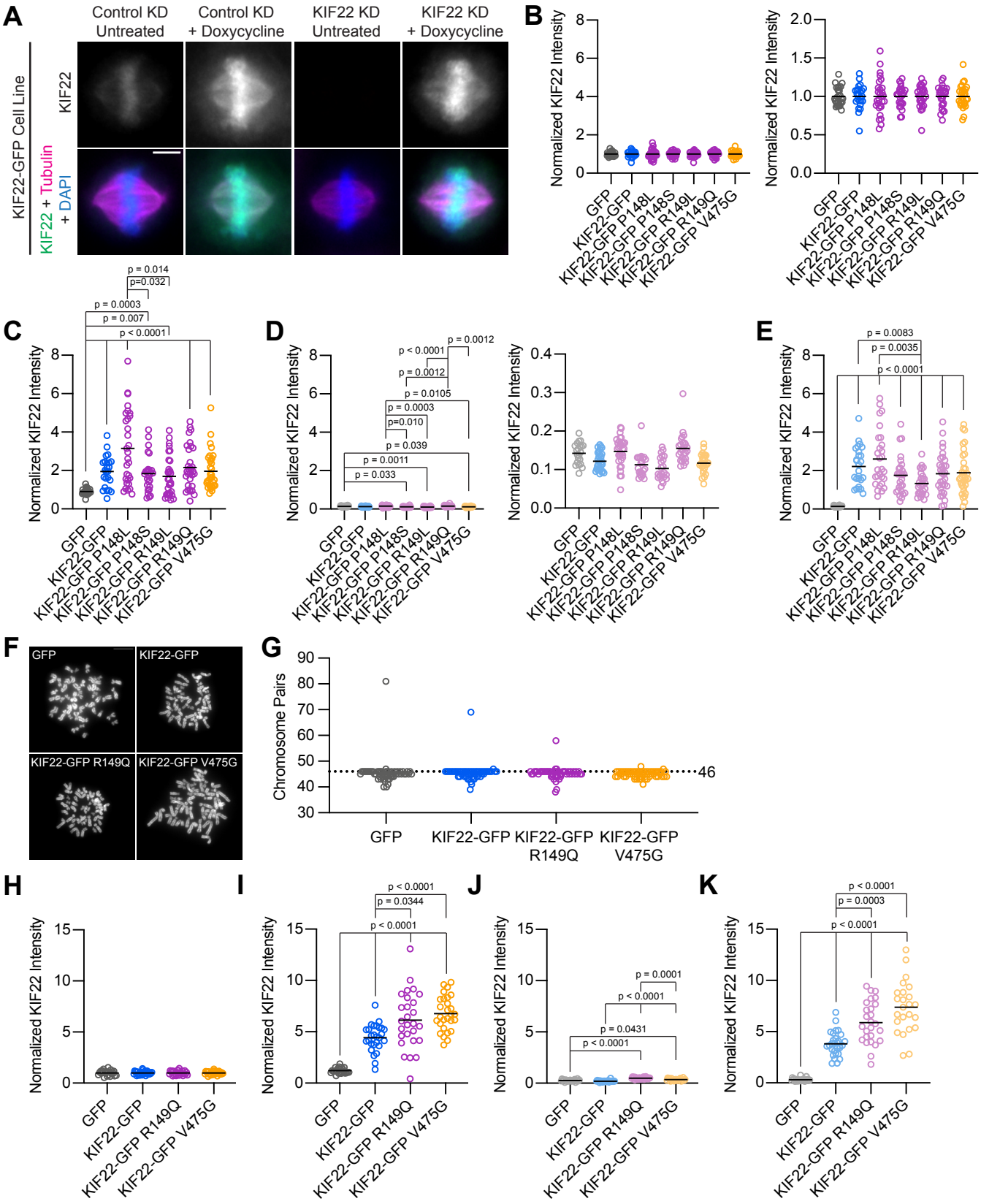

Supplemental Figure 1. HeLa-Kyoto and RPE-1 stable cell lines express mutant KIF22. **(A)** Immunofluorescence images of HeLa-Kyoto cells expressing KIF22-GFP under the control of a doxycycline inducible promoter. Images are maximum intensity projections in z of five frames at the center of the spindle. Fixed approximately 24 hours after siRNA transfection and treatment with doxycycline to induce expression. Scale bar 5 μm. KD: knockdown. **(B-E)** Quantification of KIF22 fluorescence intensity in untreated HeLa-Kyoto cells transfected with control siRNA (B), cells treated with doxycycline to induce expression and transfected with control siRNA (C), untreated cells transfected with KIF22 siRNA (D), and cells treated with doxycycline and transfected with KIF22 siRNA (E) normalized to the mean intensity of uninduced, control knockdown cells (endogenous KIF22 expression level) for each cell line (B). Data in B and D are presented with the same y-axis scale as data in C and E for comparison (left), and with independently scaled y-axes to show data variability (right). 27 GFP, 24 KIF22-GFP, 27 KIF22-GFP R149Q, 28 KIF22-GFP P148L, 25 KIF22-GFP P148S, 27 KIF22-GFP R149L, and 30 KIF22-GFP V475G untreated cells transfected with control siRNA (B), 24 GFP, 24 KIF22-GFP, 31 KIF22-GFP R149Q, 30 KIF22-GFP P148L, 27 KIF22-GFP P148S, 30 KIF22-GFP R149L, and 33 KIF22-GFP V475G doxycycline-treated cells transfected with control siRNA (C), 21 GFP, 31 KIF22-GFP, 27 KIF22-GFP R149Q, 32 KIF22-GFP P148L, 22 KIF22-GFP P148S, 22 KIF22-GFP R149L, and 25 KIF22-GFP V475G untreated cells transfected with KIF22 siRNA (D), 26 GFP, 26 KIF22-GFP, 32 KIF22-GFP R149Q, 28 KIF22-GFP P148L, 28 KIF22-GFP P148S, 27 KIF22-GFP R149L, and 33 KIF22-GFP V475G doxycycline-treated cells transfected with KIF22 siRNA (E) from 3 experiments. **(F)** DAPI-stained metaphase chromosome spreads from uninduced RPE-1 cell lines with inducible expression of GFP, KIF22-GFP, KIF22-GFP R149Q, or KIF22-GFP V475G. Scale bar 10 μm. Images are representative of 3 experiments. **(G)** Numbers of chromosome pairs counted in metaphase spreads prepared from RPE-1 stable cell lines. Dashed line indicates the expected chromosome number for diploid human cells (46). The mode for each cell line is 46. 55 GFP, 58 KIF22-GFP, 53 KIF22-GFP R149Q, and 57 KIF22-GFP V475G spreads from 3 experiments. **(H-K)** Quantification of KIF22 fluorescence intensity in untreated RPE-1 cells transfected with control siRNA (H), cells treated with doxycycline to induce expression and transfected with control siRNA (I), untreated cells transfected with KIF22 siRNA (J), and cells treated with doxycycline and transfected with KIF22 siRNA (K) normalized to the mean intensity of uninduced, control knockdown cells for each cell line (H). 23 GFP, 27 KIF22-GFP, 25 KIF22-GFP R149Q, and 27 KIF22-GFP V475G untreated cells transfected with control siRNA (H), 24 GFP, 27 KIF22-GFP, 27 KIF22-GFP R149Q, and 28 KIF22-GFP V475G doxycycline-treated cells transfected with control siRNA (I), 21 GFP, 24 KIF22-GFP, 24 KIF22-GFP R149Q, and 21 KIF22-

GFP V475G untreated cells transfected with KIF22 siRNA (J), 24 GFP, 29 KIF22-GFP, 26 KIF22-GFP R149Q, and 24 KIF22-GFP V475G doxycycline-treated cells transfected with KIF22 siRNA (K) from 3 experiments. For B-E and H-K, bars indicate means. p values from Brown-Forsythe and Welch ANOVA with Dunnett's T3 multiple comparisons test. p values are greater than 0.05 for comparisons without a marked p value.

Figure 2

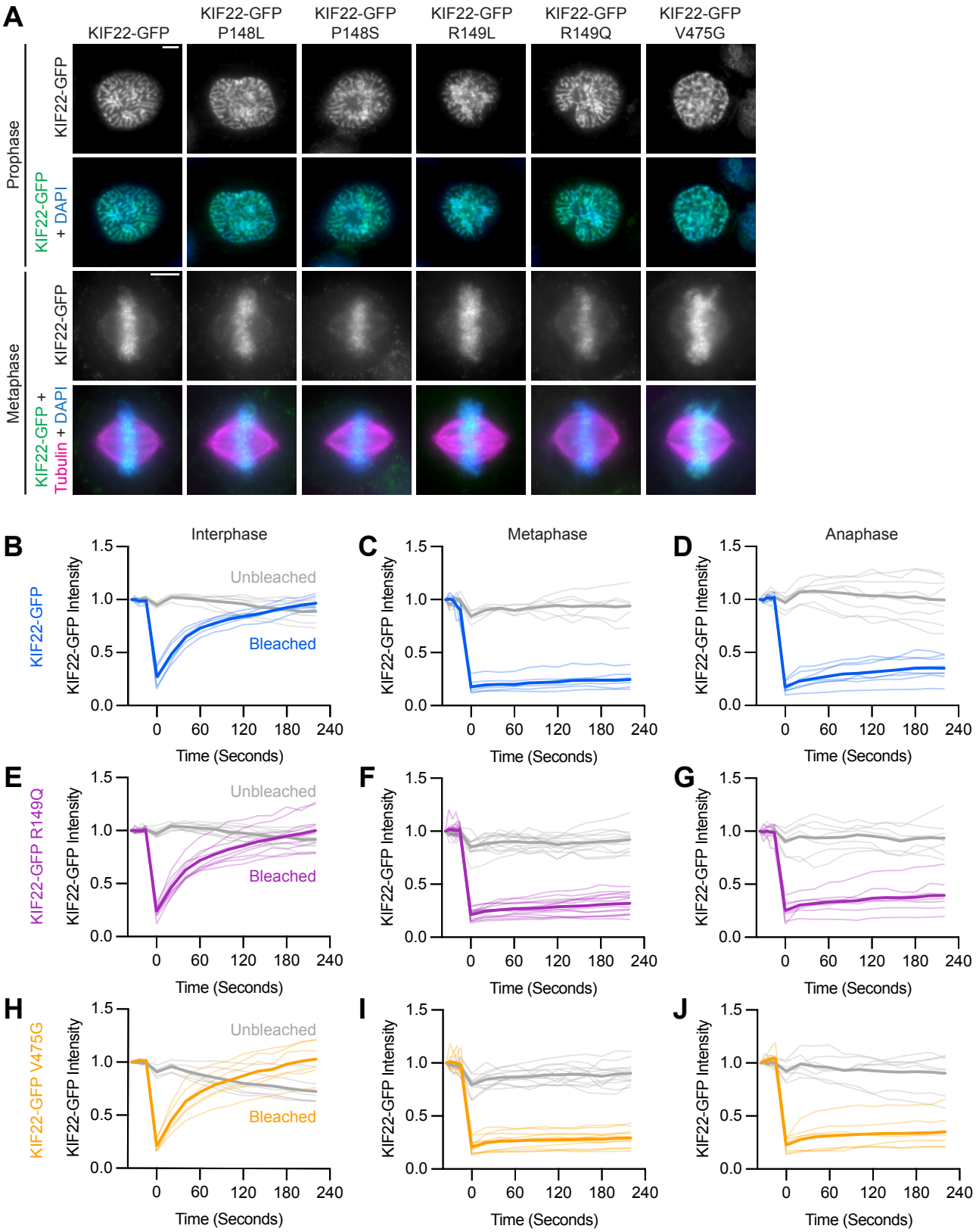

Figure 2. Pathogenic mutations in KIF22 do not disrupt the localization of the motor.

(A) Immunofluorescence images of HeLa-Kyoto cells expressing KIF22-GFP constructs in prophase (top two rows) and metaphase (bottom two rows). KIF22-GFP was visualized using an anti-GFP antibody. Images are maximum intensity projections in z of five frames at the center of the spindle (metaphase cells) or maximum intensity projections in z of two frames (prophase cells). Fixed approximately 24 hours after treatment with doxycycline to induce expression. Scale bars 5 μm. **(B-J)** Fluorescence recovery after photobleaching (FRAP) of KIF22-GFP (B-D), KIF22-GFP R149Q (E-G), and KIF22-GFP V475G (H-J) in interphase nuclei (B, E, H) or on metaphase (C, F, I) or anaphase (D, G, J) chromosomes. Bleaching occurred at time zero. Thin lines are traces from individual cells and thick lines represent means. Intensity values are normalized to the KIF22-GFP intensity in the first imaged frame before bleaching. Interphase measurements (B, E, H) obtained from 6 KIF22-GFP cells from 4 experiments, 9 KIF22-GFP R149Q cells from 5 experiments, and 6 KIF22-GFP V475G cells from 4 experiments. Metaphase measurements (C, F, I) obtained from 6 KIF22-GFP cells from 4 experiments, 14 KIF22-GFP R149Q cells from 5 experiments, and 12 KIF22-GFP V475G cells from 4 experiments. Anaphase measurements (D, G, J) obtained from 8 KIF22-GFP cells from 4 experiments, 7 KIF22-GFP R149Q cells from 5 experiments, and 7 KIF22-GFP V475G cells from 3 experiments.

Supplemental Figure 2

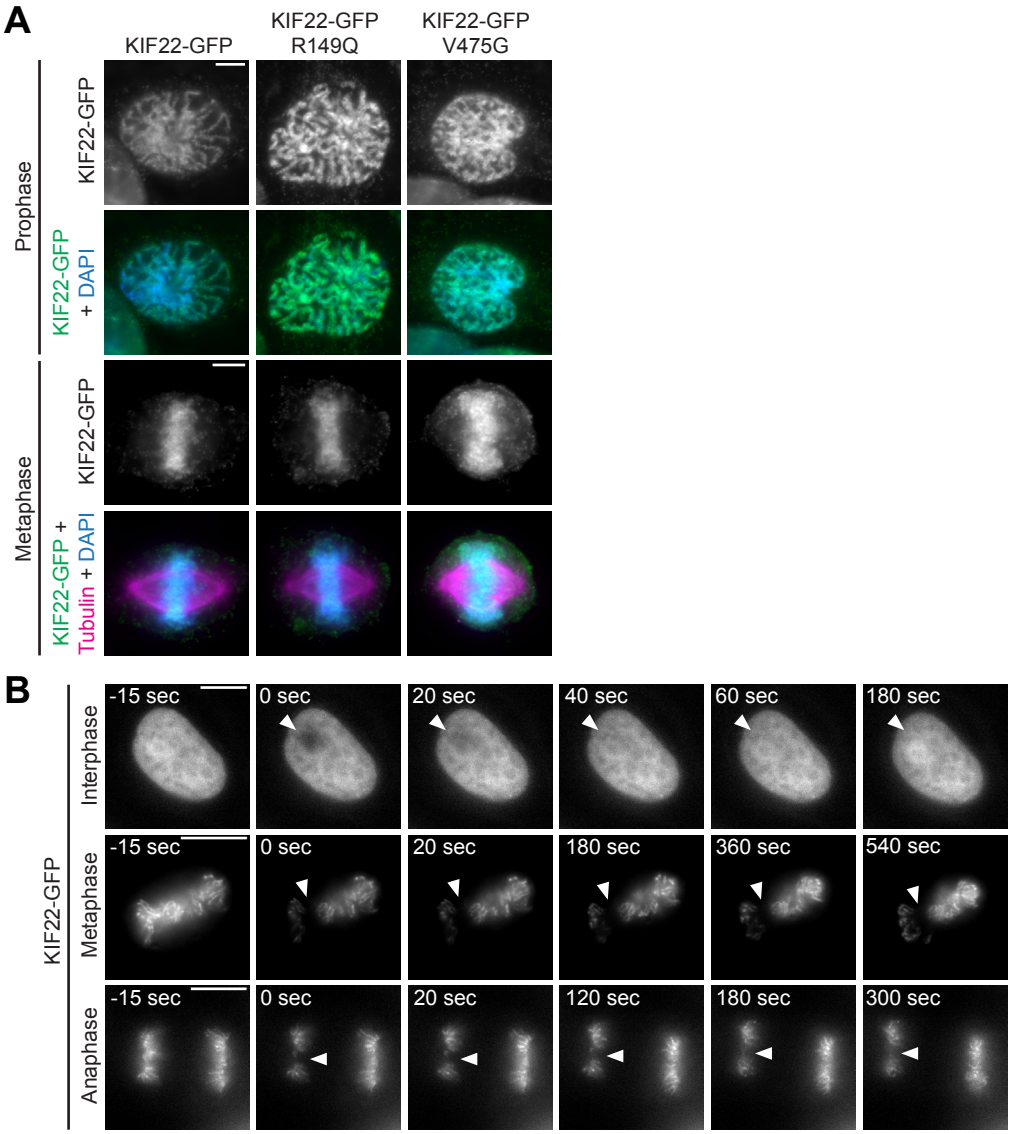

Supplemental Figure 2. Pathogenic mutations in KIF22 do not disrupt the localization of the motor in RPE-1 cells.

(A) Immunofluorescence images of RPE-1 cells expressing KIF22-GFP constructs in prophase (top two rows) and metaphase (bottom two rows). KIF22-GFP was visualized using an anti-GFP antibody. Images are maximum intensity projections in z of five frames at the center of the spindle (metaphase cells) or maximum intensity projections in z of three frames (prophase cells). Fixed approximately 18 hours after treatment with doxycycline to induce expression. Scale bars 5 μm. **(B)** Time-lapse images of fluorescence recovery after photobleaching (FRAP) in HeLa-Kyoto cells expressing KIF22-GFP. Bleaching occurred at time zero, and arrowheads indicate bleached area. Scale bars 10 μm. Images are representative of 3 or more experiments.

Mutations do not reduce polar ejection forces

In prometaphase and metaphase, KIF22 contributes to chromosome congression and alignment by generating polar ejection forces (Brouhard & Hunt, 2005; Levesque & Compton, 2001; Stumpff et al., 2012; Wandke et al., 2012). In cells treated with monastrol to inhibit Eg5/KIF11 and generate monopolar spindles, polar ejection forces push chromosomes away from a single central spindle pole (Levesque & Compton, 2001) **(Figure 3A)**. A loss of KIF22 function causes chromosomes to collapse in towards the pole in this system (Levesque & Compton, 2001) **(Figure 3A)**. To determine whether overexpression of KIF22-GFP with pathogenic mutations has a dominant effect on polar ejection force generation, wild type or mutant KIF22-GFP-expressing HeLa-Kyoto cells were treated with monastrol to induce mitotic arrest with monopolar spindles. Relative polar ejection forces were compared by measuring the distance from the spindle pole to the maximum DAPI signal **(Figure 3A)**. Expression of mutant motor did not reduce polar ejection forces **(Figure 3B and 3C)**. Rather, expression of KIF22-GFP R149L and R149Q significantly increased the distance from the pole to the maximum DAPI signal (R149L 4.6 $\pm$ 0.13 μm, R149Q 4.3 $\pm$ 0.11 μm, GFP control 3.7 $\pm$ 0.04 μm, mean $\pm$ SEM), indicating higher levels of polar ejection forces in these cells.

The same assay was used to test whether mutant KIF22 could rescue polar ejection force generation in cells depleted of endogenous KIF22. In control cells expressing GFP, depletion of endogenous KIF22 resulted in the collapse of chromosomes towards the pole **(Figure 3B)**, and the distance from the pole to the maximum DAPI signal was reduced to 1.6 $\pm$ 0.11 μm, indicating a loss of polar ejection forces **(Figure 3D)**. This reduction was not observed in cells expressing wild type or mutant KIF22-GFP, demonstrating that KIF22-GFP with pathogenic mutations is capable of generating polar ejection forces **(Figure 3B and 3D)**. In cells transfected with control siRNA and cells depleted of endogenous KIF22, polar ejection force levels did not depend on KIF22-GFP expression levels **(Figure 3E and 3F)**.

Together, the localization of mutant KIF22 and the ability of mutant KIF22 to generate polar ejection forces indicate that pathogenic mutations P148L, P148S, R149L, R149Q, and V475G do not result in a loss of KIF22 function during early mitosis.

Figure 3

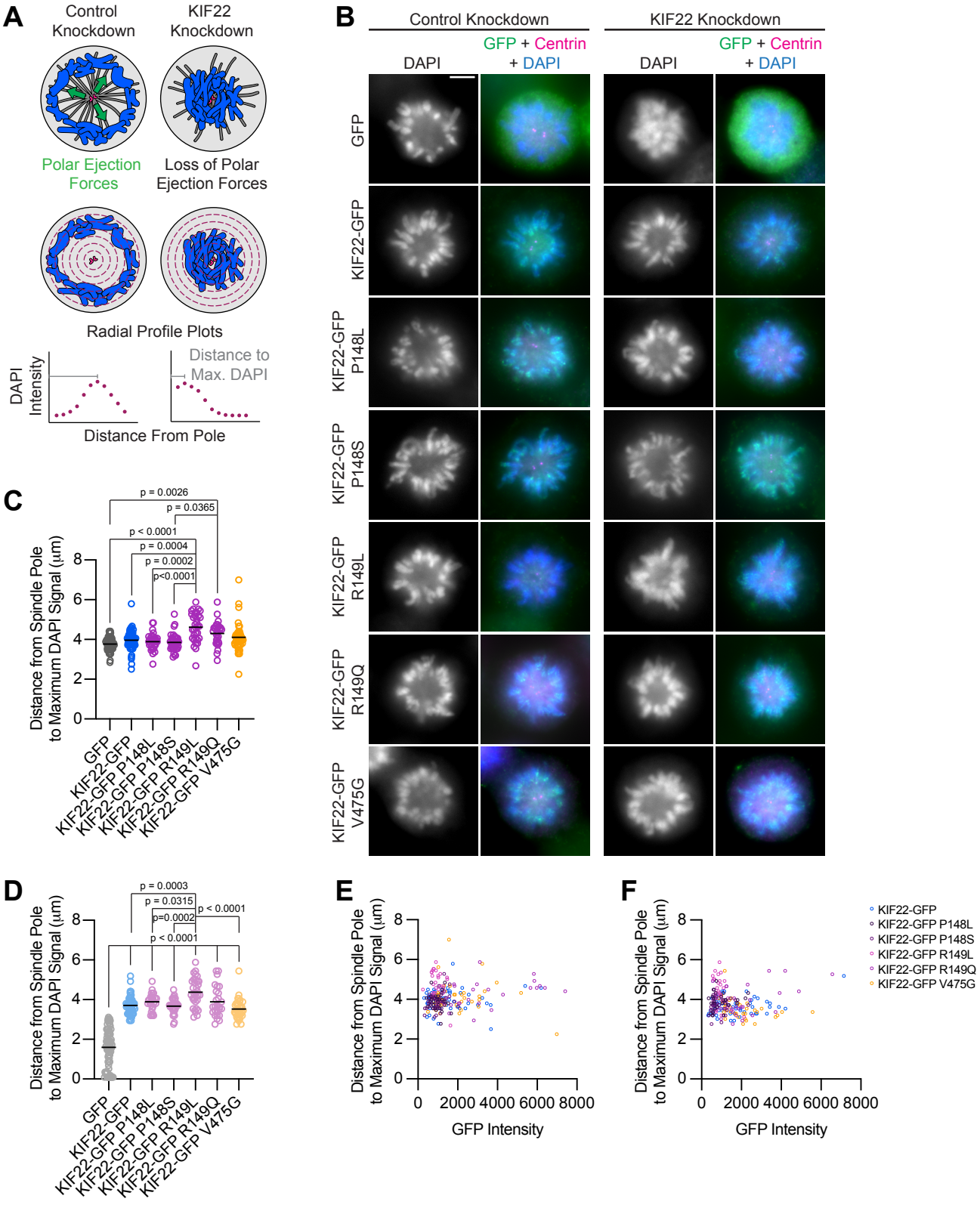

Figure 3. Pathogenic mutations in KIF22 do not reduce polar ejection forces.

(A) Schematic of changes in chromosome positions resulting from loss of polar ejection forces. In cells with monopolar spindles, both spindle poles (magenta) are positioned together and chromosomes (blue) are pushed toward the cell periphery by polar ejection forces (green) (left). In cells depleted of KIF22, polar ejection forces are reduced and chromosomes collapse in toward the center of the cell (right). Relative polar ejection forces were quantified using radial profile plots to measure the distance from the spindle pole to the maximum DAPI signal intensity. **(B)** Immunofluorescence images of monopolar HeLa-Kyoto cells. KIF22-GFP was visualized using an anti-GFP antibody. Fixed approximately 2-3 hours after treatment with monastrol and 24 hours after siRNA transfection and treatment with doxycycline to induce expression. Scale bar 5 μm. Images are representative of 3 or more experiments. **(C)** Distance from the spindle pole to the maximum DAPI signal, a measure of relative polar ejection force level, in cells transfected with control siRNA. 59 GFP cells from 7 experiments, 69 KIF22-GFP cells from 6 experiments, 31 KIF22-GFP P148L cells from 3 experiments, 37 KIF22-GFP P148S cells from 3 experiments, 33 KIF22-GFP R149L cells from 3 experiments, 28 KIF22-GFP R149Q cells from 3 experiments, and 45 KIF22-GFP V475G cells from 3 experiments. **(D)** Distance from the spindle pole to the maximum DAPI signal in cells transfected with KIF22 siRNA. 75 GFP cells from 7 experiments, 57 KIF22-GFP from 6 experiments, 28 KIF22-GFP P148L cells from 3 experiments, 30 KIF22-GFP P148S cells from 3 experiments, 33 KIF22-GFP R149L cells from 3 experiments, 26 KIF22-GFP R149Q cells from 3 experiments, and 34 KIF22-GFP V475G cells. For C-D, bars indicate means. p values from Brown-Forsythe and Welch ANOVA with Dunnett's T3 multiple comparisons test. p values are greater than 0.05 for comparisons without a marked p value. **(E-F)** Background-subtracted GFP intensity plotted against the distance from the spindle pole to the maximum DAPI signal to assess dependence of polar ejection force generation on expression levels in cells transfected with control siRNA (E) (Pearson correlation coefficient 0.105, two-tailed p value 0.1031) or KIF22 siRNA (F) (Pearson correlation coefficient -0.005, two-tailed p value 0.9427).

KIF22 mutations disrupt anaphase chromosome segregation

While pathogenic mutations did not disrupt the function of KIF22 in prometa- or metaphase, HeLa-Kyoto cells expressing mutant KIF22-GFP exhibited defects in anaphase chromosome segregation. In these cells, chromosomes did not move persistently towards the spindle poles. Instead, chromosomes began to segregate, but then reversed direction and moved back towards the center of the spindle or remained in the center of the spindle until decondensation **(Figure 4A).** This phenotype was dominant and occurred in the presence of endogenous KIF22. Recongression was quantified by measuring the distance between separating chromosome masses as anaphase progressed. In cells expressing wild type KIF22-GFP, this value increases steadily and then plateaus. Expression of mutant KIF22-GFP causes the distance between chromosome masses to increase, then decrease as chromosomes recongress, and then increase again as segregation continues **(Figure 4B)**. Recongression reduces the distance between chromosome masses 7 minutes after anaphase onset in cells expressing KIF22-GFP with pathogenic mutations (median distance 2.0 – 7.2 μm) compared to cells expressing wild type KIF22-GFP (median distance 12.9 μm) **(Figure 4C)**. Defects in anaphase chromosome segregation were also observed in RPE-1 cells expressing KIF22-GFP R149Q or V475G **(Figure S3D, S3E, S3F)**. This gain of function phenotype is consistent with a lack of KIF22 inactivation in anaphase, resulting in a failure to suspend polar ejection force generation.

If recongression is the result of increased KIF22 activity in anaphase, we would predict that increased levels of KIF22-GFP expression would cause more severe anaphase chromosome segregation defects. Indeed, plotting the distance between chromosome masses 7 minutes after anaphase onset against mean GFP intensity for each HeLa-Kyoto cell demonstrated that these two values were correlated (Spearman correlation coefficient -0.6246, one-tailed p value < 0.0001) **(Figure S3A)**. Considering only cells expressing lower levels of KIF22-GFP (mean background subtracted intensity <100 arbitrary units) emphasized the differences in the distance between chromosome masses as anaphase progressed between cells expressing wild type and mutant motor **(Figure S3B, S3C)**.

In a subset of HeLa-Kyoto cells, expression of KIF22-GFP with pathogenic mutations caused cytokinesis failure **(Figure 4D)**. This result is consistent with the published observation that causing chromosome recongression by preventing cyclin B1 degradation can result in cytokinesis failure (Wolf et al., 2006). In cells expressing KIF22-GFP with pathogenic mutations, cleavage furrow ingression began, but did not complete, resulting in a single daughter cell. The percentage of cells failing to complete cytokinesis was approximately ten-fold higher in cells

383 expressing mutant KIF22-GFP (R149Q 36%, V475G 25%) than in cells expressing wild type
384 KIF22-GFP (3%). Additionally, the distance between chromosome masses at the time of cleavage
385 furrow ingression was reduced in cells expressing KIF22-GFP R149Q or V475G, suggesting that
386 the position of the chromosome masses may be physically obstructing cytokinesis **(Figure 4E)**.
387 Consistent with this hypothesis, cells that failed to complete cytokinesis tended to have lower
388 distances between chromosome masses than the distances measured in cells in which
389 cytokinesis completed despite expression of mutant KIF22-GFP **(Figure 4E)**.

Figure 4

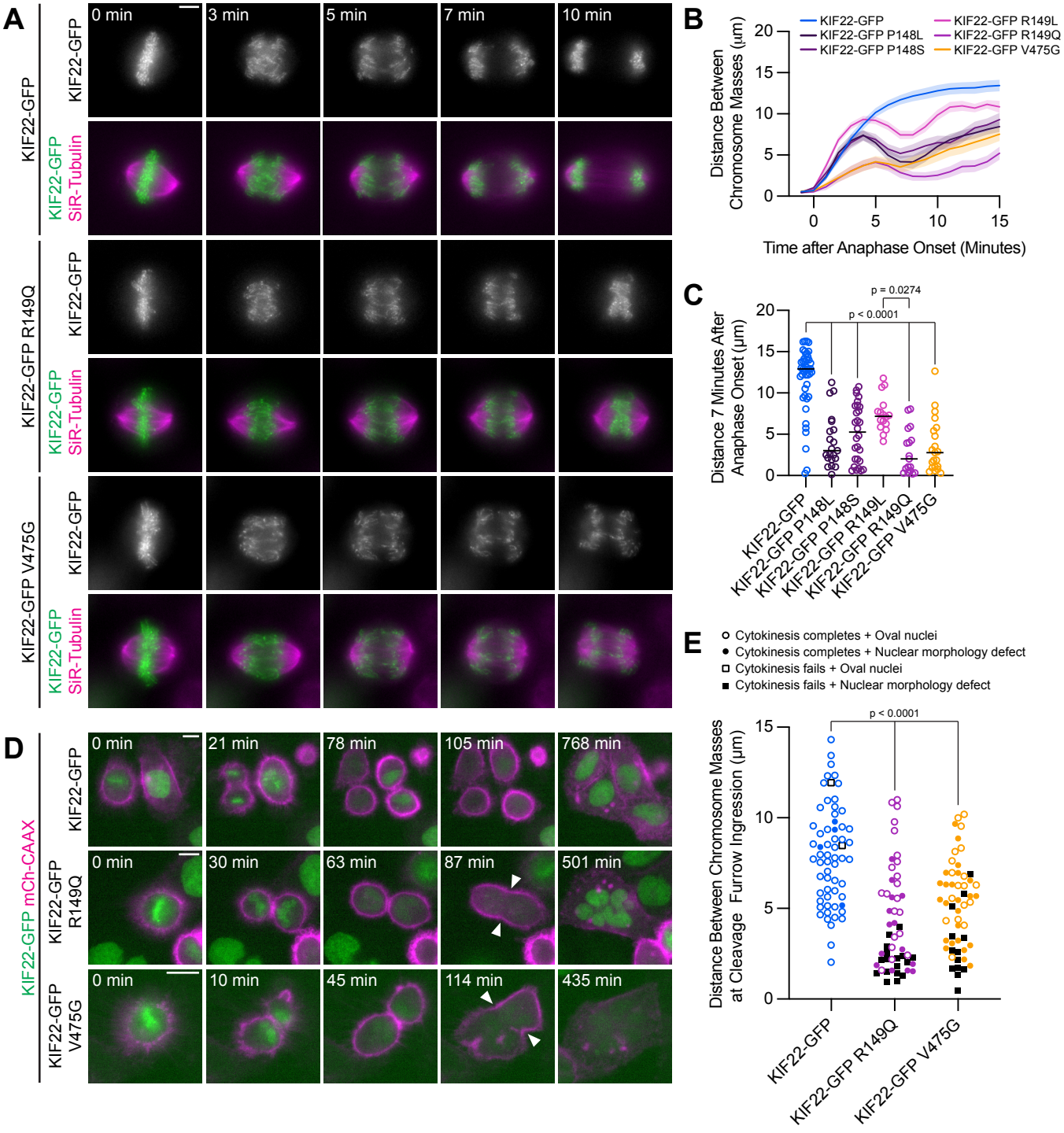

Figure 4. Pathogenic mutations in KIF22 disrupt anaphase chromosome segregation.
(A) Time-lapse images of dividing HeLa-Kyoto cells expressing KIF22-GFP R149Q or KIF22-GFP V475G. Times indicate minutes after anaphase onset. Images are maximum intensity projections in z through the entirety of the spindle. Imaged approximately 18 hours after treatment with doxycycline to induce expression. Scale bar 5 μm. Images are representative of 3 or more experiments. **(B)** Distance between separating chromosome masses throughout anaphase in HeLa-Kyoto cells. Lines represent the mean and the shaded area denotes SEM. 43 KIF22-GFP cells from 10 experiments, 21 KIF22-GFP P148L cells from 6 experiments, 28 KIF22-GFP P148S cells from 7 experiments, 16 KIF22-GFP R149L cells from 6 experiments, 17 KIF22-GFP R149Q cells from 4 experiments, and 21 KIF22-GFP V475G cells from 21 experiments. **(C)** Distance between separating chromosome masses 7 minutes after anaphase onset. Bars indicate medians. p values from Kruskal-Wallis test. p values are greater than 0.05 for comparisons without a marked p value. Data represent the same cell populations presented in (B). **(D)** Time-lapse images of dividing HeLa-Kyoto cells expressing mCherry (mCh)-CAAX to visualize cell boundaries. Times indicate minutes after anaphase onset. Arrowheads indicate cytokinesis failure. Imaged approximately 8 hours after treatment with doxycycline to induce expression and 24-32 hours after transfection with mCh-CAAX. Scale bars 20 μm. Images are representative of 3 or more experiments. **(E)** Distance between chromosome masses at the time of cleavage furrow ingression. p values from Kruskal-Wallis test. p values are greater than 0.05 for comparisons without a marked p value. 62 KIF22-GFP cells from 10 experiments, 52 KIF22-GFP R149Q cells from 9 experiments, and 55 KIF22-GFP V475G cells from 9 experiments.

Supplemental Figure 3

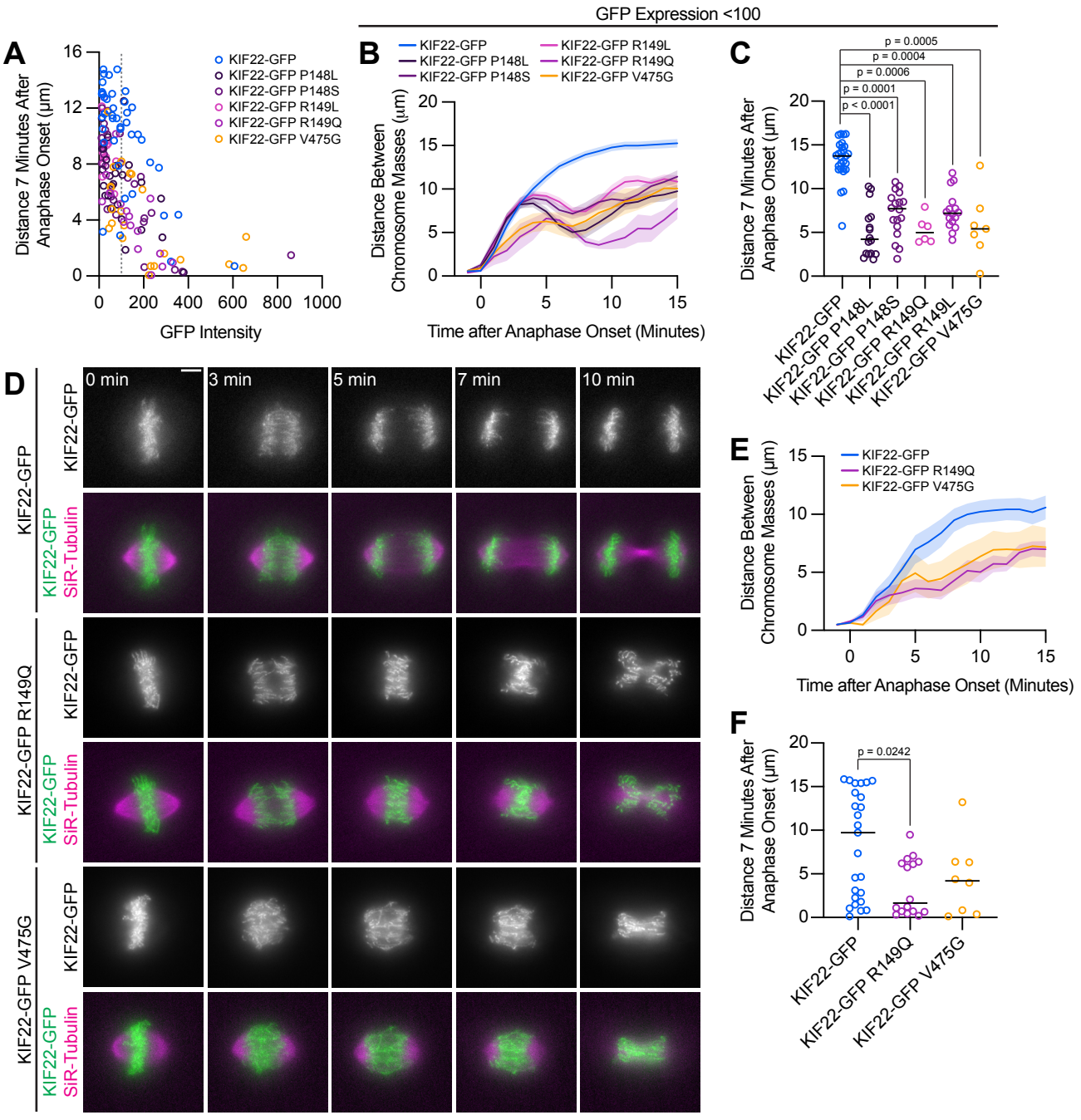

Supplemental Figure 3. Anaphase recongression defects are KIF22-GFP expression level dependent and disrupt chromosome segregation in RPE1 cells.

(A) Background-subtracted GFP intensity plotted against the distance between separating chromosome masses at 7 minutes to assess dependence of recongression on expression level (Spearman correlation coefficient -0.6246, one-tailed p value < 0.0001). Grey dashed line indicates mean background subtracted GFP intensity of 100. 43 KIF22-GFP cells from 10 experiments, 21 KIF22-GFP P148L cells from 6 experiments, 28 KIF22-GFP P148S cells from 7 experiments, 16 KIF22-GFP R149L cells from 6 experiments, 17 KIF22-GFP R149Q cells from 4 experiments, and 21 KIF22-GFP V475G cells from 21 experiments. **(B)** Distance between separating chromosome masses of cells expressing lower levels of KIF22-GFP (mean background subtracted GFP intensity less than 100). Lines represent the mean and the shaded area denotes SEM. 27 KIF22-GFP cells from 9 experiments, 16 KIF22-GFP P148L cells from 6 experiments, 18 KIF22-GFP P148S cells from 6 experiments, 16 KIF22-GFP R149L cells from 6 experiments, 6 KIF22-GFP R149Q cells from 3 experiments, and 7 KIF22-GFP V475G cells from 3 experiments. **(C)** Distance between separating chromosome masses 7 minutes after anaphase onset of cells expressing lower levels of KIF22-GFP (mean background subtracted GFP intensity less than 100). Bars indicate medians. p values from Kruskal-Wallis test. p values are greater than 0.05 for comparisons without a marked p value. Data represent the same cell populations presented in (B). **(D)** Time-lapse images of dividing RPE-1 cells expressing KIF22-GFP R149Q or KIF22-GFP V475G. Imaged approximately 12-18 hours after treatment with doxycycline to induce expression. Times indicate minutes after anaphase onset. Images are maximum intensity projections in z through the entirety of the spindle. Scale bar 5 μm. Images are representative of 3 or more experiments. **(E)** Distance between separating chromosome masses throughout anaphase in RPE-1 cells. Lines represent the mean and the shaded area denotes SEM. 25 KIF22-GFP cells from 7 experiments, 16 KIF22-GFP R149Q cells from 6 experiments, and 8 KIF22-GFP V475G cells from 6 experiments. **(F)** Distance between separating chromosome masses 7 minutes after anaphase onset in RPE-1 cells. Bars indicate medians. p value from Kruskal-Wallis test. p values are greater than 0.05 for comparisons without a marked p value. Data represent the same cell populations presented in (E).

Mutations disrupt the separation of the spindle poles in anaphase

Anaphase chromosome segregation requires both that chromosome arms and centromeres move towards the spindle poles (anaphase A) (Asbury, 2017) and that the spindle poles move away from one another (anaphase B) (Ris, 1949). To test whether the activity of mutant KIF22 in anaphase affects one or both of these processes, anaphase was imaged in HeLa-Kyoto cells expressing fluorescent markers for the poles (pericentrin-RFP) and centromeres (CENPB-mCh) **(Figure 5A)**. The reduced distance between separating chromosome masses seen in these cells **(Figure 5B, 5C)** was compared to the distances between the centromeres **(Figure 5D, 5E)** and the distances between the poles **(Figure 5F, 5G)** as anaphase progressed. The distances between all three structures showed the same trend: in cells expressing wild type KIF22-GFP, the distance between chromosome masses, between centromeres, and between the spindle poles increased throughout the measured time interval in anaphase. Pathogenic mutations altered the movements of all three structures **(Figure 5B, 5D, 5F)**. The distance between chromosome masses, between centromeres, and between the spindle poles 10 minutes after anaphase onset was significantly reduced in cells expressing KIF22-GFP R149Q or KIF22-GFP V475G **(Figure 5C, 5E, 5G)**. Comparing the distance between chromosome masses and the spindle pole within each half spindle **(Figure 5H)** with the distance between centromeres and the spindle pole in the same half spindles **(Figure 5I)** demonstrated that expression of mutant KIF22 more potently reduced the segregation of chromosome arms than centromeres, consistent with continued generation of polar ejection forces in anaphase. This suggests that pathogenic mutations in KIF22 affect anaphase A by altering the movement of chromosome arms, but not the shortening of the k-fibers, and affect anaphase B by altering spindle pole separation.

Figure 5

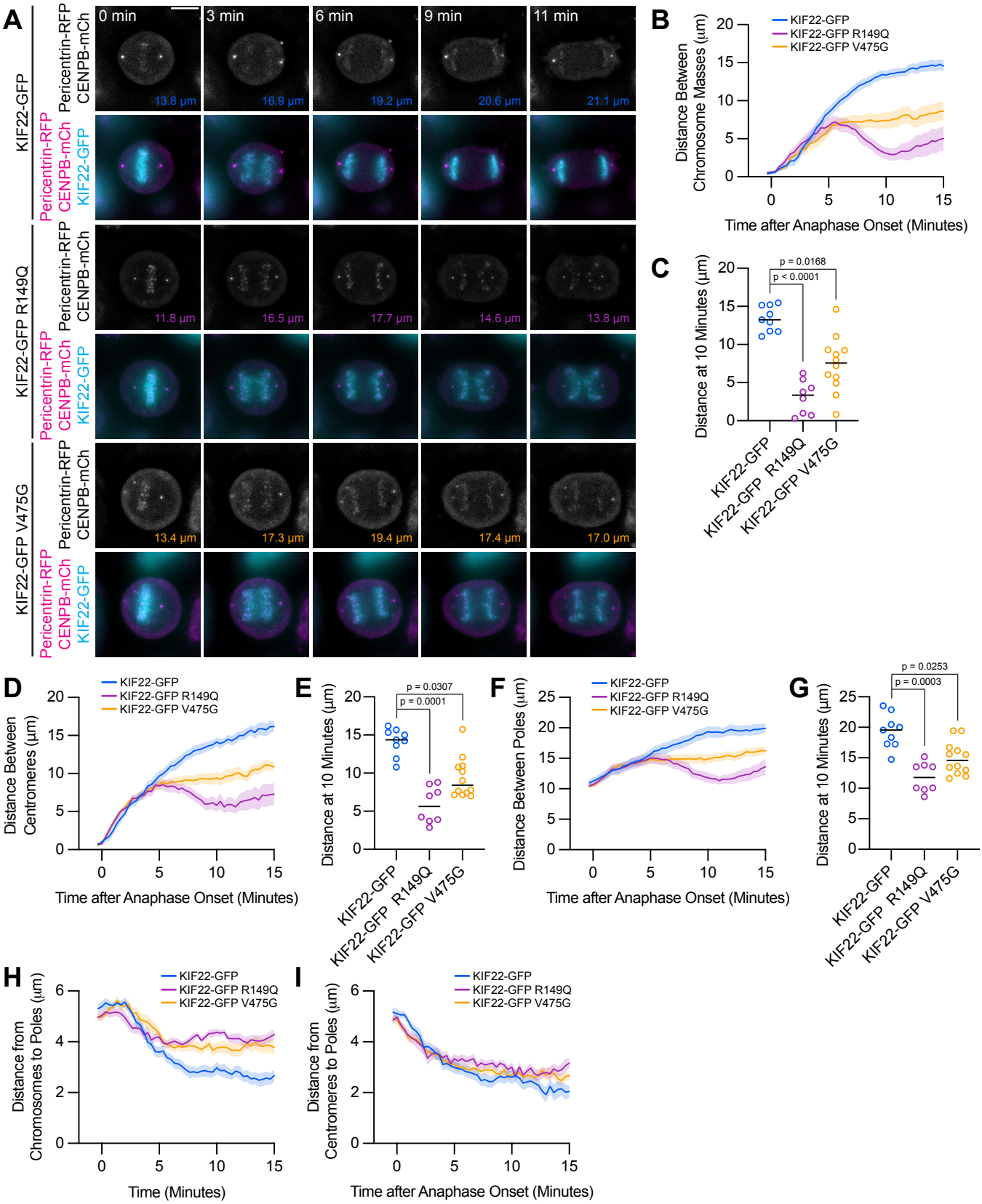

Figure 5. Mutations disrupt the separation of spindle poles in anaphase.

(A) Time-lapse images of dividing HeLa-Kyoto cells expressing pericentrin-RFP to mark the spindle poles and CENPB-mCh to mark centromeres. Times indicate minutes after anaphase onset. Colored distances in the bottom right of each greyscale image indicate the distance between the spindle poles in the image. Images are maximum intensity projections in z through the entirety of the spindle. Imaged approximately 24 hours after transfection and 12-18 hours after treatment with doxycycline to induce expression. Images depicting pericentrin-RFP and CENPB-mCh signal were background subtracted by duplicating each frame, applying a gaussian blur (sigma 30 pixels), and subtracting this blurred image from the original. Scale bar 10 μm. Images are representative of 3 or more experiments. **(B)** Distance between separating chromosome masses throughout anaphase in HeLa-Kyoto cells. Lines represent the mean and the shaded area denotes SEM. **(C)** Distance between separating chromosome masses 10 minutes after anaphase onset in HeLa-Kyoto cells. Bars indicate medians. **(D)** Distance between centromeres (CENPB-mCh) throughout anaphase in HeLa-Kyoto cells. Lines represent the mean and the shaded area denotes SEM. **(E)** Distance between centromeres 10 minutes after anaphase onset in HeLa-Kyoto cells. Bars indicate medians. **(F)** Distance between spindle poles (pericentrin-RFP) throughout anaphase in HeLa-Kyoto cells. Lines represent the mean and the shaded area denotes SEM. **(G)** Distance between spindle poles 10 minutes after anaphase onset in HeLa-Kyoto cells. Bars indicate medians. Measurements from the same cells (9 KIF22-GFP cells from 5 experiments, 8 KIF22-GFP R149Q cells from 4 experiments, and 12 KIF22-GFP V475G cells from 6 experiments) are shown in B-G. For C, E, and G, p values from Kruskal-Wallis test. **(H)** Distance between chromosome masses and spindle poles throughout anaphase in HeLa-Kyoto cells. Lines represent the mean and the shaded area denotes SEM. **(I)** Distance between centromeres and spindle poles throughout anaphase in HeLa-Kyoto cells. Lines represent the mean and the shaded area denotes SEM. Measurements from the same cells (18 KIF22-GFP, 16 KIF22-GFP R149Q, and 24 KIF22-GFP V475G half-spindles) as in B-G are shown in H and I.

Division of cells expressing KIF22 with pathogenic mutations results in daughter cells with abnormally shaped nuclei

To understand the consequences of the observed defects in anaphase chromosome segregation, we examined the daughter cells produced by the division of cells expressing KIF22-GFP with pathogenic mutations. In these cells, the nuclei are lobed and fragmented **(Figure 6A)**. The percentage of divisions resulting in nuclear morphology defects was approximately ten-fold higher than in control cells (KIF22-GFP 6%, KIF22-GFP R149Q 64%, KIF22-GFP V475G 68%) when live divisions were observed **(Figure 4E)**. To further quantify this phenotype, the solidity of fixed cell nuclei (the ratio of the area of each nucleus to the area of the convex shape that would enclose it) was measured. A perfectly oval nucleus would have a solidity value of one. Solidity values were reduced in cells expressing KIF22-GFP with pathogenic mutations **(Figure 6B)**, indicating that these cells had more irregularly shaped nuclei. This reduction in solidity was dominant and occurred both in the presence of endogenous KIF22 and when endogenous KIF22 was depleted via siRNA knockdown. Using the fifth percentile solidity of control cells (control knockdown, GFP expression) as a cut-off, 44-63% of cells expressing mutant KIF22-GFP had abnormally shaped nuclei 24 hours after treatment with doxycycline to induce expression of KIF22-GFP **(Figure 6C)**. Expression of wild type KIF22-GFP also resulted in a small increase in the percentage of cells with abnormally shaped nuclei (12%). This percentage was reduced when endogenous KIF22 was depleted (7%), consistent with nuclear morphology defects resulting from an increase in KIF22 activity.

Expression of KIF22-GFP with pathogenic mutations also caused abnormally shaped nuclei in RPE-1 cells **(Figure S4A)**. The solidity of nuclei in cells expressing mutant KIF22-GFP was reduced **(Figure S4B)**, and 40-49% of RPE-1 cells expressing mutant KIF22-GFP had abnormally shaped nuclei, again defined as a solidity value less than the fifth percentile of control cells **(Figure 4C)**. In RPE-1 cells, expression of wild type KIF22-GFP resulted in a higher percentage of cells with abnormally shaped nuclei (18% in control knockdown cells, 15% with KIF22 knockdown) than was seen in HeLa-Kyoto cells. This may be a result of the higher expression level of KIF22-GFP in the RPE-1 inducible cell lines **(Figure S1I, S1K)**.

To determine whether these nuclear morphology defects depended on the ability of KIF22 to generate forces within the mitotic spindle, cells were treated with nocodazole to depolymerize microtubules and reversine to silence the spindle assembly checkpoint, allowing cells to enter and exit mitosis without assembling a spindle or segregating chromosomes (Samwer et al., 2017; Serra-Marques et al., 2020) **(Figure 6D)**. The solidity of nuclei was measured before chromosomes condensed **(Figure 6E)** and after mitotic exit **(Figure 6F)**. At both time points, there

was no difference in nuclear shape between control cells and cells expressing KIF22-GFP with pathogenic mutations, indicating that the effects of mutations on nuclear structure are spindle-dependent.

The effect of nuclear morphology defects on daughter cell fitness may partially depend on whether the nuclear envelopes of abnormally shaped nuclei are intact. The expression of mCherry (mCh) with a nuclear localization signal (NLS) indicated that even highly lobed and fragmented nuclei in cells expressing mutant KIF22-GFP are capable of retaining nuclear-localized proteins **(Figure 6G)**. This suggests that the nuclear envelopes of these abnormally shaped nuclei are still intact enough to function as a permeability barrier (Hatch, Fischer, Deerinck, & Hetzer, 2013).

Figure 6

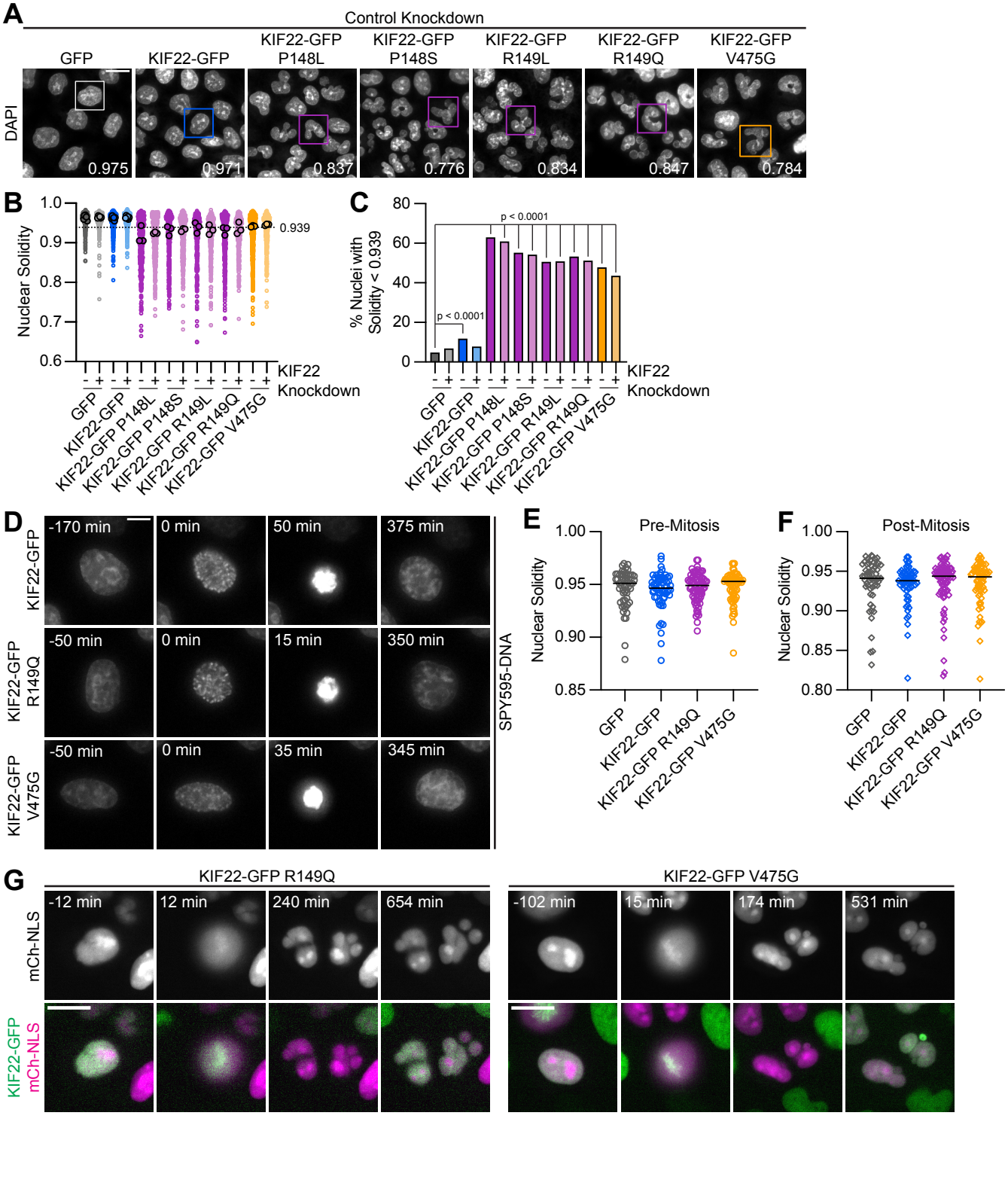

Figure 6: Division of cells expressing KIF22 with pathogenic mutations results in daughter cells with abnormally shaped nuclei.

(A) DAPI stained nuclei of cells expressing KIF22 with pathogenic mutations. Values in the bottom right of each image indicate the solidity of the boxed nucleus. Fixed approximately 24 hours after treatment with doxycycline to induce expression. Scale bar 20 μm. Images are representative of 3 or more experiments. **(B)** Measured solidity of nuclei in HeLa-Kyoto cell lines. Small circles represent the solidity of individual nuclei, and large circles with black outlines indicate the median of each experiment. A dashed line marks a solidity value of 0.939, the fifth percentile of solidity for control cells transfected with control siRNA and expressing GFP. **(C)** Percentage of nuclei with abnormal shape, indicated by a solidity value less than 0.939, the fifth percentile of control (control knockdown, GFP expression) cell solidity. A chi-square test of all data produced a p value < 0.0001. Plotted p values are from pairwise post-hoc chi-square tests comparing control (control knockdown, GFP expression) cells to each other condition. Applying the Bonferroni correction for multiple comparisons, a p value of less than 0.00385 was considered significant. p values are greater than 0.00385 for comparisons without a marked p value. Data in (B) and (C) represent 1045 GFP cells transfected with control siRNA, 849 GFP cells transfected with KIF22 siRNA, 994 KIF22-GFP cells transfected with control siRNA, 980 KIF22-GFP cells transfected with KIF22 siRNA, 472 KIF22-GFP P148L cells transfected with control siRNA, 442 KIF22-GFP P148L cells transfected with KIF22 siRNA, 382 KIF22-GFP P148S cells transfected with control siRNA, 411 KIF22-GFP P148S cells transfected with KIF22 siRNA, 336 KIF22-GFP R149L cells transfected with control siRNA, 376 KIF22-GFP R149L cells transfected with KIF22 siRNA, 466 KIF22-GFP R149Q cells transfected with control siRNA, 359 KIF22-GFP R149Q cells transfected with KIF22 siRNA, 605 KIF22-GFP V475G cells transfected with control siRNA, and 386 KIF22-GFP V475G cells transfected with KIF22 siRNA. GFP and KIF22-GFP cells represent 6 experiments, data from all other cell lines represent 3 experiments. **(D)** Time-lapse images of HeLa-Kyoto cells treated with nocodazole and reversine and stained with SPY595-DNA to visualize chromosomes. Time indicates the number of minutes before or after chromosome condensation. Images are maximum intensity projections in z of two focal planes, one at the level of interphase nuclei and one at the level of mitotic chromosomes. Imaged approximately 8 hours after treatment with doxycycline to induce expression, 1.5-2 hours after treatment with SPY595-DNA, and 0.5-1 hour after treatment with nocodazole and reversine. Scale bar 10 μm. Images are representative of 3 or more experiments. **(E)** Nuclear solidity of HeLa-Kyoto cells treated with nocodazole and reversine. Measurements were made 15 minutes before chromosome condensation. **(F)** Nuclear solidity of HeLa-Kyoto cells treated with nocodazole and reversine. Measurements were made

100 minutes after chromosome decondensation. Data in (E) and (F) represent 56 GFP, 60 KIF22-GFP, 76 KIF22-GFP R149Q, and 67 KIF22-GFP V475G cells from 3 experiments per condition. For (E) and (F), bars indicate medians, and the Kruskal-Wallis test indicated no significant difference between groups. **(G)** Time-lapse images of HeLa-Kyoto cells expressing mCherry (mCh)-NLS to assess nuclear envelope integrity. Times indicate minutes before or after chromosome condensation. Imaged approximately 8 hours after treatment with doxycycline to induce expression and 24 hours after transfection with mCh-CAAX. Scale bar 20 μm. Images are representative of 3 or more experiments.

Supplemental Figure 4

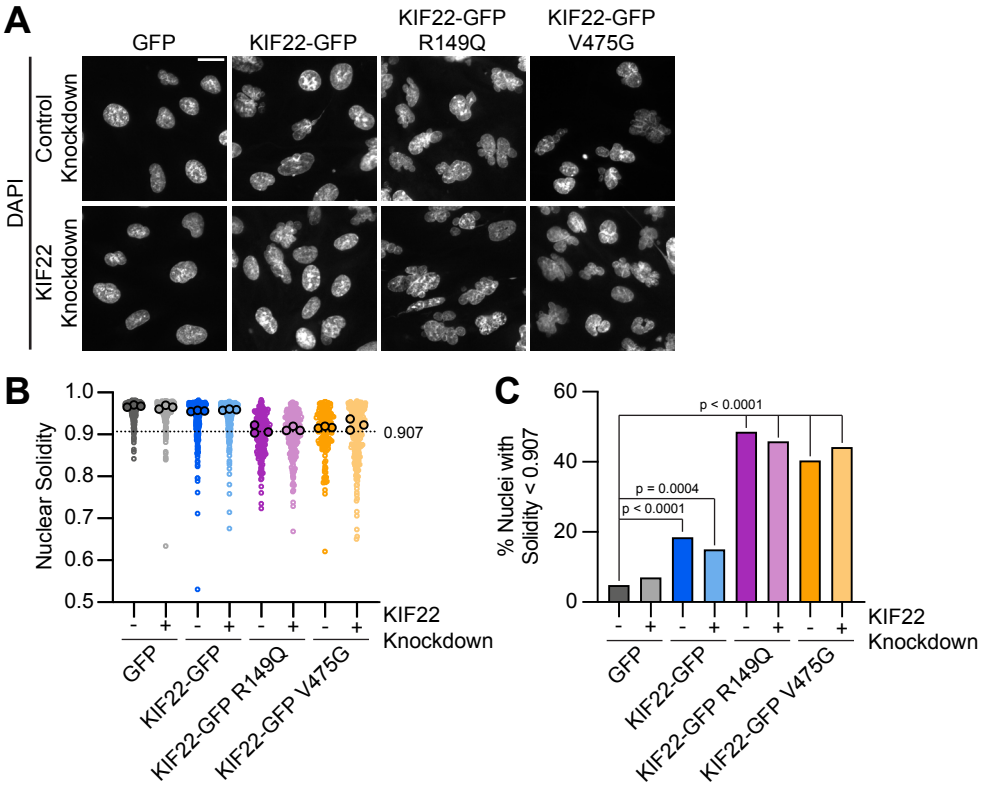

Supplemental Figure 4: Mutations cause abnormally shaped nuclei in RPE1 cells.

(A) DAPI-stained nuclei of RPE-1 cells expressing KIF22-GFP with pathogenic mutations. Fixed approximately 24 hours after treatment with doxycycline to induce expression. Scale bar 20 μm. Images are representative of 3 or more experiments. **(B)** Measured solidity of nuclei in RPE-1 cell lines. Small circles represent the solidity of individual nuclei, and large circles with black outlines indicate the median of each experiment. A dashed line marks a solidity value of 0.907, the fifth percentile of solidity for control cells transfected with control siRNA and expressing GFP. **(C)** Percentage of nuclei with abnormal shape, indicated by a solidity value less than 0.907, the fifth percentile of control (control knockdown, GFP expression) cell solidity. A chi-square test of all data produced a p value < 0.0001. Plotted p values are from pairwise post-hoc chi-square tests comparing control (control knockdown, GFP expression) cells to each other condition. Applying the Bonferroni correction for multiple comparisons, a p value of less than 0.00714 was considered significant. p values are greater than 0.00714 for comparisons without a marked p value. Data in (B) and (C) represent 206 GFP transfected with control siRNA, 200 GFP cells transfected with KIF22 siRNA, 233 KIF22-GFP cells transfected with control siRNA, 240 KIF22-GFP cells transfected with KIF22 siRNA, 214 KIF22-GFP R149Q cells transfected with control siRNA, 207 KIF22-GFP R149Q cells transfected with KIF22 siRNA, 146 KIF22-GFP V475G cells transfected with control siRNA, and 244 KIF22-GFP V475G cells transfected with KIF22 siRNA from 3 experiments.

Proliferation is reduced in cells expressing KIF22 with pathogenic mutations

If defects in anaphase chromosome segregation and nuclear morphology affect cellular function, they may impact the ability of cells to proliferate. To test this, HeLa-Kyoto cells expressing KIF22-GFP with pathogenic mutations were imaged over 96 hours to count the numbers of cells over time **(Figure 7A)**. The growth rates of cells expressing mutant KIF22 were reduced **(Figure 7B)**. After 96 hours, the fold change in cell number was reduced by approximately 30% for cells expressing KIF22-GFP with pathogenic mutations (GFP control median 5.3, KIF22-GFP R149Q 3.7, KIF22-GFP V475G 3.8) **(Figure 7C)**.

To consider what might be limiting the proliferation rate of cells expressing mutant KIF22-GFP, predictions for proliferation rate based on the observed rates of nuclear morphology defects and cytokinesis failure were calculated. For these purposes, only data from the first 48 hours of the proliferation assay were used, as cell growth rates plateaued after this timepoint. The doubling time of control HeLa-Kyoto cells expressing GFP was calculated to be 20.72 hours in these experiments, which is consistent with published data (Y. Liu et al., 2018). Using this doubling rate, assuming exponential growth, and assuming every cell divides, the normalized cell count at 48 hours (normalized to a starting cell count of 1) was predicted to be 4.98. This is close to the experimental 48-hour cell count for control cells (4.60), and higher than the experimental 48-hour cell count for cells expressing KIF22-GFP R149Q (3.13) or V475G (3.60), as these cell lines have reduced proliferation **(Figure 7B, square)**. If one assumed that cells with abnormally shaped nuclei stop dividing, given that approximately 60% of mutant KIF22-GFP cell divisions result in abnormally shaped nuclei **(Figure 4E),** the predicted cell count at 48 hours would be 2.18 **(Figure 7B, triangle)**. This is lower than the experimental cell count for cells expressing mutant KIF22-GFP, suggesting that cells with abnormally shaped nuclei must be capable of additional divisions. If, instead, one assumed that only cells that fail cytokinesis (30% of cells **(Figure 4E)**) stop dividing, the predicted cell count would be 3.42 **(Figure 7B, diamond)**. This value is consistent with the experimental 48-hour cell count for cells expressing KIF22-GFP with pathogenic mutations (3.13 – 3.60), suggesting the rate of cytokinesis failure may limit the rate of proliferation in these cells. Consistent with this possibility, an increased number of large cells that may have failed cytokinesis are visible in proliferation assay images at 72 hours **(Figure 7A)**.

To test the prediction that cells with nuclear morphology defects are capable of division, KIF22-GFP expression was induced approximately 24 hours before imaging to generate a population of cells with abnormally shaped nuclei. Division of these cells was observed **(Figure 7D)**, demonstrating that nuclear morphology defects do not prevent subsequent divisions. The percentage of cells that divided over the course of this experiment was not reduced in cells

626 expressing KIF22-GFP with pathogenic mutations despite the abnormal nuclear morphology of
627 cells in those populations **(Figure 7E)**.

Figure 7

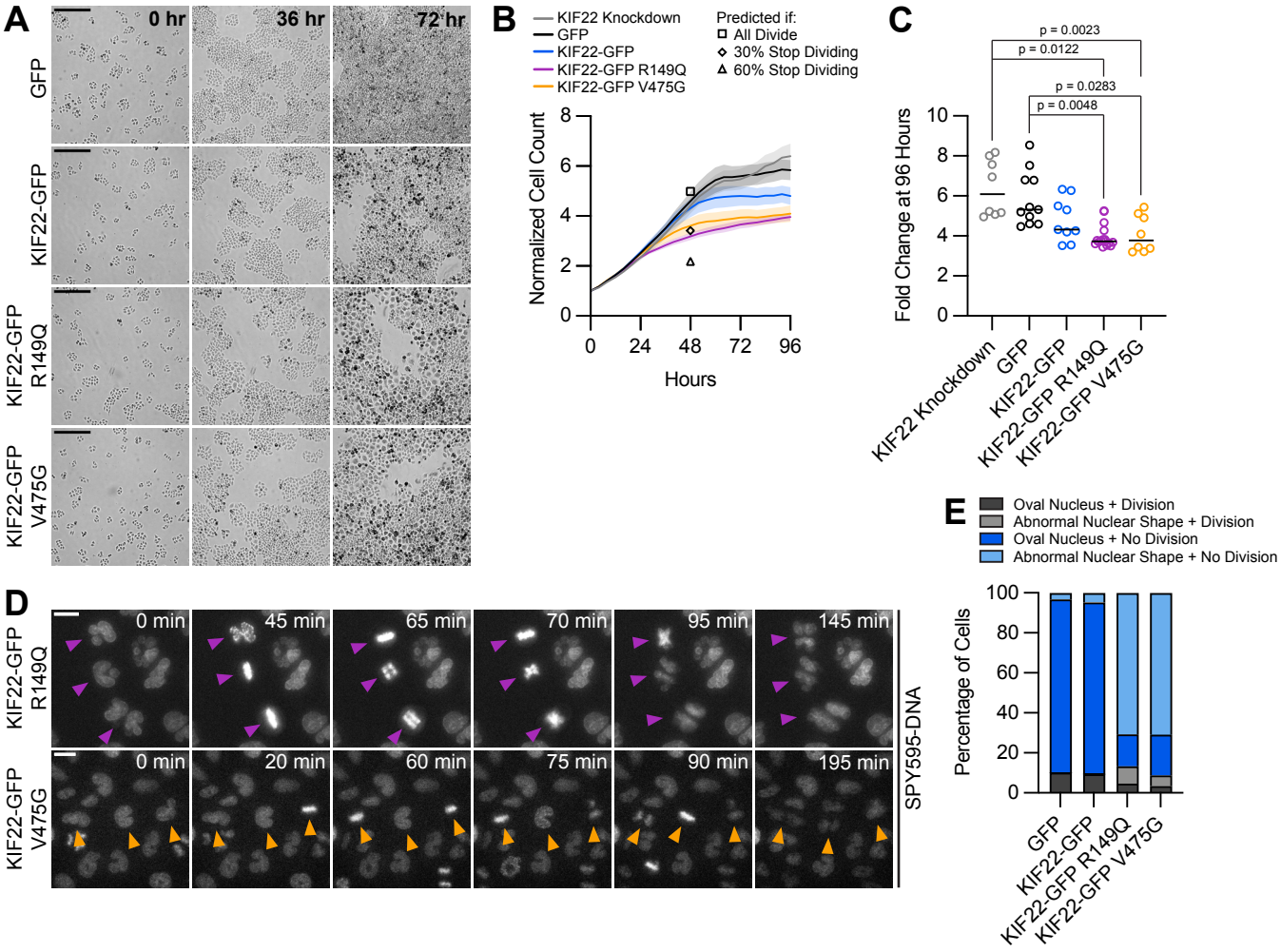

Figure 7: Proliferation is reduced in cells expressing KIF22 with pathogenic mutations. **(A)** Time-lapse bright field images of HeLa-Kyoto cells to assess proliferation rate. Scale bar 500 μm. Images are representative of 3 or more experiments. **(B)** Proliferation rates measured using automated bright field imaging. Lines represent the mean cell count, normalized to the number of cells at 0 hours, and the shaded area denotes SEM. Black outlined shapes indicate the predicted cell count for cell lines expressing pathogenic mutations at 48 hours if every cell doubled every 20.72 hours (the doubling time measured from 48 hours of control cell proliferation) (square), if the rate of cytokinesis failure limited proliferation and 30% of cells did not divide (diamond), and if the rate of nuclear morphology defects limited proliferation and 60% of cells did not divide (triangle). **(C)** Fold change of normalized cell counts after 96 hours. Bars indicate medians. p values from Kruskal-Wallis test. p values are greater than 0.05 for comparisons without a marked p value. Data in (B) and (C) represent 8 KIF22 knockdown, 11 GFP, 9 KIF22-GFP, 16 KIF22-GFP R149Q, and 8 KIF22-GFP V475G technical replicates from 4 experiments. **(D)** Time-lapse imaging of HeLa-Kyoto cells treated with doxycycline for 24 hours to induce expression of KIF22-GFP with pathogenic mutations and stained with SPY595-DNA. Arrowheads indicate cells with abnormally shaped nuclei that divide. Images are maximum intensity projections in z of two focal planes, one at the level of interphase nuclei and one at the level of mitotic chromosomes. Scale bars 20 μm. Images are representative of 3 or more experiments. **(E)** Nuclear morphology at the start of imaging (dark grey or blue, oval; light grey or blue; abnormal morphology) and outcome (grey, cell divides during the experiment; blue, the cell does not divide). The total number of dividing cells was compared between cell lines using the chi-square test ($p < 0.0001$ across all conditions). Post-hoc chi-square tests comparing all conditions to one another indicated that the proliferation rate of cells expressing KIF22-GFP R149Q is statistically different than that of cells expressing GFP ($p = 0.0025$), KIF22-GFP ($p = 0.0003$), or KIF22-GFP V475G ($p < 0.0001$). Applying the Bonferroni correction for multiple comparisons, a p value of less than 0.008 was considered significant. p values are greater than 0.008 for all other comparisons. 2461 GFP, 2611 KIF22-GFP, 1890 KIF22-GFP R149Q, and 2346 KIF22-GFP V465G cells.

Mimicking phosphorylation of T463 phenocopies pathogenic mutations

The phenotypes observed in cells expressing KIF22-GFP with pathogenic mutations suggest that mutations may prevent inactivation of KIF22 in anaphase, and that polar ejection forces in anaphase disrupt chromosome segregation. If this is the case, then preventing KIF22 inactivation would be predicted to phenocopy the pathogenic mutations. One mechanism by which KIF22 activity is controlled is phosphorylation of T463: phosphorylation of this tail residue is necessary for polar ejection force generation, and dephosphorylation at anaphase onset contributes to polar ejection force suppression (Soeda et al., 2016). Therefore, we generated HeLa-Kyoto inducible cell lines expressing KIF22-GFP with phosphomimetic (T463D) and phosphonull (T463A) mutations to test whether preventing KIF22 inactivation in anaphase by expressing the constitutively active T463D construct phenocopies the expression of KIF22-GFP with pathogenic mutations. When treated with doxycycline, these cells expressed phosphomimetic and phosphonull KIF22-GFP at levels comparable to those seen in cell lines expressing KIF22-GFP with pathogenic mutations, which was approximately two- to three-fold higher than the level of expression of endogenous KIF22 **(Figure S5A-D)**.

To assess the activity of KIF22-GFP T463D and T463A in HeLa cells, polar ejection force generation in monopolar spindles was measured **(Figure 8A)**. In cells with endogenous KIF22 present, expression of KIF22-GFP T463D increased the distance from the spindle pole to the maximum DAPI signal (GFP control 3.7 ± 0.07 μm, KIF22-GFP T463D 4.4 ± 0.12, mean ± SEM), indicating increased polar ejection forces, consistent with phosphorylation of T463 activating KIF22 in prometaphase (Soeda et al., 2016) **(Figure 8B)**. Conversely, when endogenous KIF22 was depleted, expression of KIF22-GFP T463A was less able to rescue polar ejection force generation (distance from the spindle pole to the maximum DAPI signal 3.0 ± 0.08 μm, mean ± SEM) than expression of wild type KIF22-GFP (3.6 ± 0.07 μm) or KIF22-GFP T463D (3.7 ± 0.10 μm) **(Figure 8C)**. Again, this is consistent with previous work demonstrating that KIF22 phosphorylation at T463 activates the motor for prometaphase polar ejection force generation (Soeda et al., 2016), although the reduction in polar ejection forces seen with KIF22-GFP T463A rescue is less severe in our system, possibly due to differences in cell type, level of depletion of endogenous KIF22, or the method used to quantify polar ejection forces.

In anaphase, expression of phosphomimetic KIF22-GFP T463D, but not phosphonull KIF22-GFP T463A, caused chromosome recongression **(Figure 8D, 8E)**. The distance between chromosome masses at 7 minutes was reduced in cells expressing KIF22-GFP T463D (median 5.8 μm) compared to cells expressing wild type KIF22-GFP (12.5 μm) or KIF22-GFP T463A (10.8 μm) **(Figure 8F)**. As in cells expressing KIF22-GFP with pathogenic mutations, the severity of

anaphase chromosome recongression, indicated by the distance between chromosome masses at 7 minutes, was dependent on GFP expression level (Spearman correlation coefficient -0.3964, one-tailed p value 0.0004) **(Figure S5E)**. When only cells expressing lower levels of KIF22-GFP (mean background subtracted intensity <100 arbitrary units) were considered, the same effect (expression of KIF22-GFP T463D causes recongression) was still observed **(Figure S5F, S5G)**. This recongression phenocopies the effect of pathogenic mutations on anaphase chromosome segregation, consistent with pathogenic mutations preventing anaphase inactivation of KIF22.

In addition to causing the same defects in anaphase chromosome segregation, expression of KIF22-GFP T463D also affects daughter cell nuclear morphology. Cells expressing KIF22-GFP T463D have lobed and fragmented nuclei **(Figure S5H)** and correspondingly reduced nuclear solidity measurements **(Figure 8G)**. An increased percentage of cells expressing KIF22-GFP T463D in the presence of endogenous KIF22 (65%) or in cells depleted of endogenous KIF22 (72%) have abnormally shaped nuclei, as indicated by a solidity value below the fifth percentile of control cell nuclear solidity **(Figure 8H)**.

Expression of KIF22-GFP T463A also resulted in a small increase in the percentage of abnormally shaped nuclei (26% in control or KIF22 knockdown conditions) **(Figure 8H)**. Since expression of KIF22-GFP T463A does not cause anaphase recongression **(Figure 8E)**, the level of compaction of the segregating chromosome masses was explored as a possible explanation for this modest increase in the percentage of cells with nuclear morphology defects. In KIF22 knockout mice, loss of KIF22 reduces chromosome compaction in anaphase, causing the formation of multinucleated cells (Ohsugi et al., 2008). The phosphonull T463A mutation reduces KIF22 activity and may therefore exhibit a KIF22 loss of function phenotype. Measurement of the widths of separating chromosome masses in anaphase **(Figure S5I)** did demonstrate a modest broadening of the chromosome masses in cells expressing KIF22-GFP T463A **(Figure S5J, S5K)**, which may contribute to the modest defects in nuclear morphology seen in these cells.

Figure 8

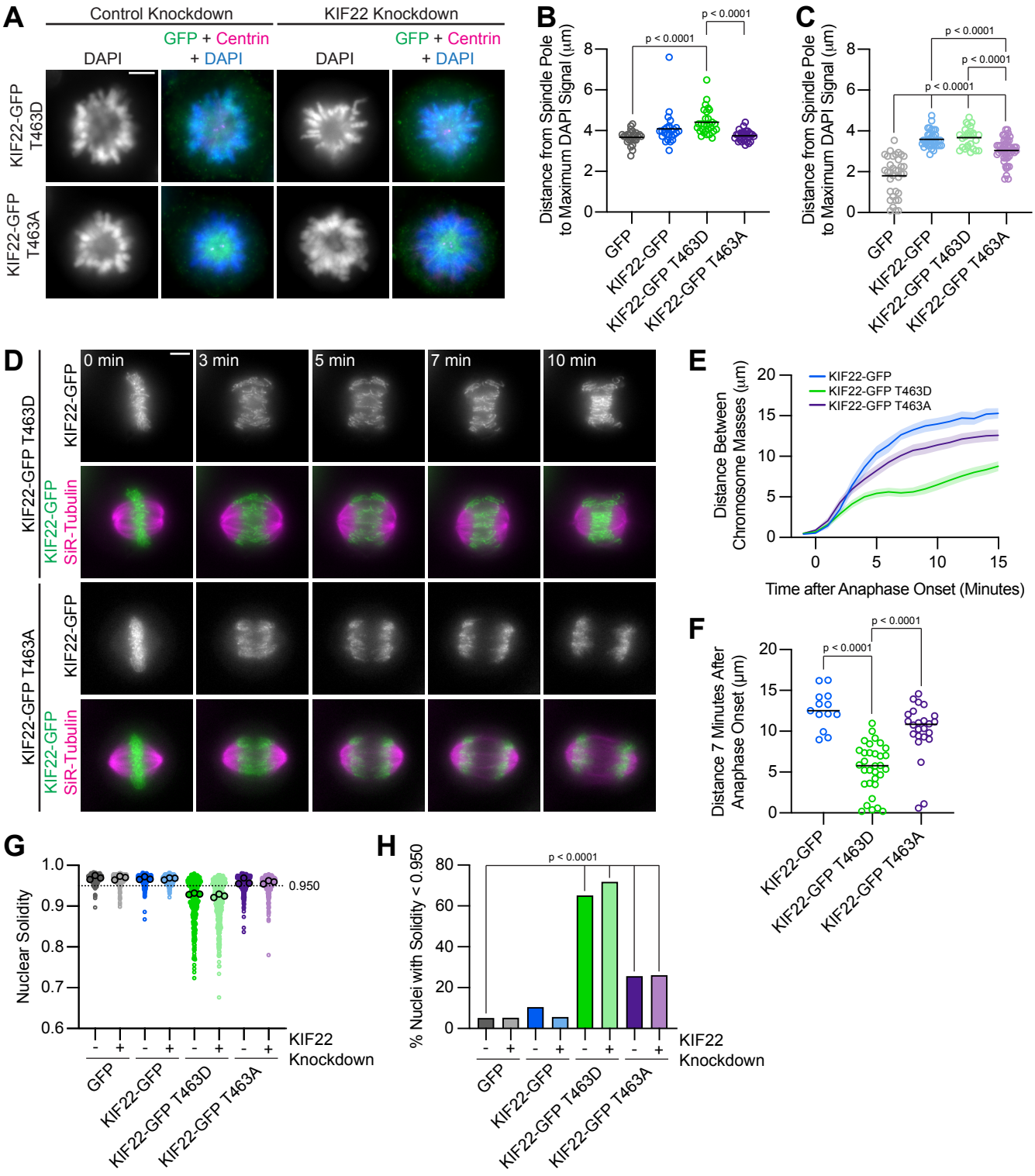

Figure 8: Phosphomimetic mutation of T463 phenocopies pathogenic mutations in KIF22. **(A)** Immunofluorescence images of monopolar HeLa-Kyoto cells. KIF22-GFP was visualized using an anti-GFP antibody. Fixed approximately 2-3 hours after treatment with monastrol and 24 hours after siRNA transfection and treatment with doxycycline to induce expression. Scale bar 5 μm. Images are representative of 3 or more experiments. **(B)** Distance from the spindle pole to the maximum DAPI signal, a measure of relative polar ejection force level, between HeLa-Kyoto cell lines expressing KIF22-GFP with phosphomimetic and phosphonull mutations at T463. 26 GFP cells from 3 experiments, 26 KIF22-GFP cells from 3 experiments, 29 KIF22-GFP T463D cells from 3 experiments, and 29 KIF22-GFP T463A cells from 3 experiments. **(C)** Distance from the spindle pole to the maximum DAPI signal in cells depleted of endogenous KIF22 and expressing KIF22-GFP with phosphomimetic and phosphonull mutations at T463. 35 GFP cells from 4 experiments, 36 KIF22-GFP cells from 4 experiments, 27 KIF22-GFP T463D cells from 3 experiments, and 47 KIF22-GFP T463A cells from 4 experiments. For B-C, bars indicate means. p values from Brown-Forsythe and Welch ANOVA with Dunnett's T3 multiple comparisons test. p values are greater than 0.05 for comparisons without a marked p value. **(D)** Time-lapse images of dividing HeLa-Kyoto cells. Cells expressing KIF22-GFP T463D exhibit recongression of the chromosomes during anaphase. Times indicate minutes after anaphase onset. Images are maximum intensity projections in z through the entirety of the spindle. Imaged approximately 18 hours after treatment with doxycycline to induce expression. Scale bar 5 μm. Images are representative of 3 or more experiments. **(E)** Distance between separating chromosome masses throughout anaphase in HeLa-Kyoto cells. Lines represent the mean and the shaded area denotes SEM. 13 KIF22-GFP, 32 KIF22-GFP T463D, and 24 KIF22-GFP T463A cells from 5 experiments. **(F)** Distance between separating chromosome masses 7 minutes after anaphase onset. Bars indicate medians. p values from Kruskal-Wallis test. p values are greater than 0.05 for comparisons without a marked p value. 13 KIF22-GFP, 32 KIF22-GFP T463D, and 24 KIF22-GFP T463A cells from 5 experiments per condition. **(G)** Measured solidity of nuclei in HeLa-Kyoto cell lines. Small circles represent the solidity of individual nuclei, and large circles with black outlines indicate the median of each experiment. A dashed line marks a solidity value of 0.950, the fifth percentile of solidity for control cells transfected with control siRNA and expressing GFP. **(H)** Percentage of nuclei with abnormal shape, indicated by a solidity value less than 0.950, the fifth percentile of control (control knockdown, GFP expression) cell solidity. A chi-square test of all data produced a p value < 0.0001. Plotted p values are from pairwise post-hoc chi-square tests comparing control (control knockdown, GFP expression) cells to each other condition. Applying

747 the Bonferroni correction for multiple comparisons, a p value of less than 0.00714 was considered
748 significant. p values are greater than 0.00714 for comparisons without a marked p value. Data in
749 (G) and (H) represent 312 GFP cells transfected with control siRNA, 362 GFP cells transfected
750 with KIF22 siRNA, 314 KIF22-GFP cells transfected with control siRNA, 320 KIF22-GFP cells
751 transfected with KIF22 siRNA, 361 KIF22-GFP T463D cells transfected with control siRNA, 376
752 KIF22-GFP T463D cells transfected with KIF22 siRNA, 312 KIF22-GFP T463A cells transfected
753 with control siRNA, and 376 KIF22-GFP T463A cells transfected with KIF22 siRNA from 3
754 experiments.

Supplemental Figure 5

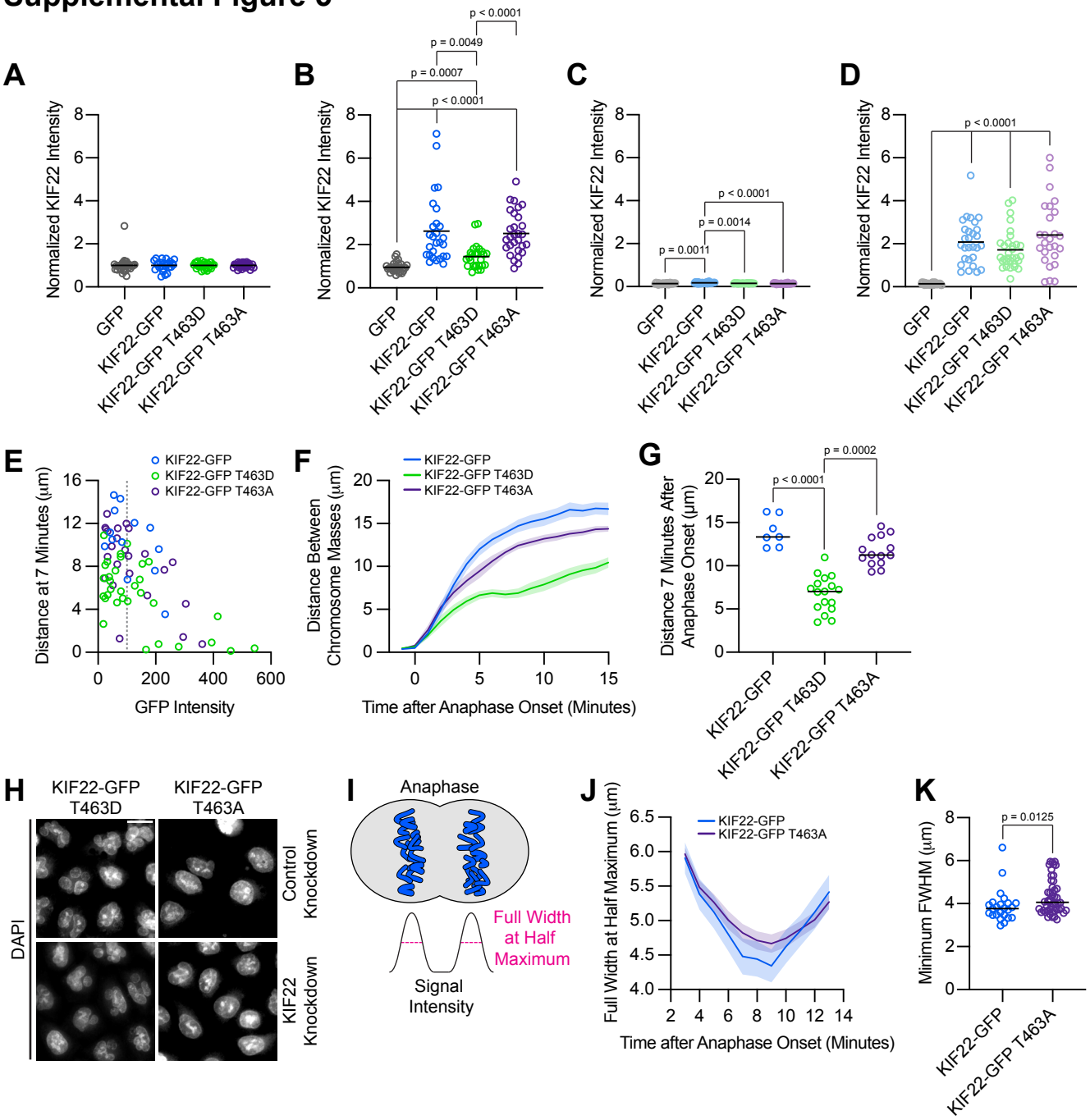

Supplemental Figure 5: Cells expressing KIF22-GFP T463A have broader anaphase chromosome masses.

(A-D) Quantification of KIF22 fluorescence intensity in untreated HeLa-Kyoto cells transfected with control siRNA (A), cells treated with doxycycline to induce expression and transfected with control siRNA (B), untreated cells transfected with KIF22 siRNA (C), and cells treated with doxycycline and transfected with KIF22 siRNA (D) normalized to the mean intensity of uninduced, control knockdown cells (endogenous KIF22 expression level) for each cell line (A). 32 GFP, 25 KIF22-GFP,28 KIF22-GFP T463D, and 31 KIF22-GFP T463A untreated cells transfected with control siRNA (A), 29 GFP, 27 KIF22-GFP, 27 KIF22-GFP T463D, and 29 KIF22-GFP T463A doxycycline-treated cells transfected with control siRNA (B), 25 GFP, 26 KIF22-GFP, 23 KIF22-GFP T463D, and 26 KIF22-GFP T463A untreated cells transfected with KIF22 siRNA (C), 28 GFP, 28 KIF22-GFP, 31 KIF22-GFP T463D, and 26 KIF22-GFP T463A doxycycline-treated cells transfected with KIF22 siRNA (D), from 3 experiments. **(E)** Plotting background-subtracted GFP intensity against the distance between separating chromosome masses at 7 minutes indicates that this distance is dependent on expression level (Spearman correlation coefficient -0.3964, one-tailed p value = 0.0004). Grey dashed line indicates mean background subtracted GFP intensity of 100. 13 KIF22-GFP, 32 KIF22-GFP T463D, and 24 KIF22-GFP T463A cells from 5 experiments. **(F)** Distance between separating chromosome masses of cells expressing lower levels of KIF22-GFP (mean background subtracted GFP intensity less than 100). Lines represent the mean and the shaded area denotes SEM. 7 KIF22-GFP cells from 4 experiments, 17 KIF22-GFP T463D cells from 5 experiments, and 14 KIF22-GFP T463A cells from 4 experiments. **(G)** Distance between separating chromosome masses 7 minutes after anaphase onset of cells expressing lower levels of KIF22-GFP (mean background subtracted GFP intensity less than 100). Bars indicate medians. p values from Kruskal-Wallis test. p values are greater than 0.05 for comparisons without a marked p value. 7 KIF22-GFP cells from 4 experiments, 17 KIF22-GFP T463D cells from 5 experiments, and 14 KIF22-GFP T463A cells from 4 experiments. **(H)** DAPI-stained nuclei of Hela-Kyoto cells. Fixed approximately 24 hours after treatment with doxycycline to induce expression. Scale bar 20 μm. Images are representative of 3 or more experiments. **(I)** Schematic depicting the measurement of chromosome signal intensity in anaphase and the use of the full width at half maximum (FWHM) as a measure of anaphase chromosome mass broadness. **(J)** Full width at half maximum of the plotted intensities of separating chromosome masses of HeLa-Kyoto cells expressing KIF22-GFP or KIF22-GFP T463A. Lines represent the mean and the shaded area denotes SEM. **(K)** Minimum FWHM value, representing maximal anaphase chromosome compaction, between cells expressing KIF22-GFP and KIF22-GFP

T463A. p value from Mann-Whitney test. Bars represent medians. Data in (J) and (K) represent 12 KIF22-GFP and 24 KIF22-GFP T463A cells (24 KIF22-GFP and 48 KIF22-GFP T463A chromosome masses) from 5 experiments.

Mimicking phosphorylation of T158 in the α2 helix phenocopies pathogenic mutations

The effect of mutations in the α2 helix on KIF22 function suggests the involvement of this region of the motor domain in KIF22 inactivation. If this was true, post-translational modification of α2 may contribute to the regulation of KIF22 activity, analagous to the regulation of KIF22 inactivation via the dephosphorylation of T463 in the tail. Phosphorylation of amino acids T134 in α2a (Kettenbach et al., 2011) and T158 in α2b (Olsen et al., 2010; Rigbolt et al., 2011) has been documented in phosphoproteomic studies. HeLa-Kyoto cells expressing KIF22-GFP with phosphomimetic and phosphonull mutations at T134 and T158 were generated to test whether either site may contribute to the regulation of KIF22 inactivation.

T134 is located in α2a, near the catalytic site of KIF22 **(Figure S6A)**. Both phosphonull (T134A) and phosphomimetic (T134D) mutations at this site disrupted the localization of KIF22. KIF22-GFP T134D and T134A localize to spindle microtubules rather than to the chromosomes **(Figure S6B)**. Expression of KIF22-GFP T134D and KIF22-GFP T134A also resulted in the formation of multipolar spindles in a subset of cells **(Figure S6C)**. These phenotypes are consistent with previous work that used T134N as a rigor mutation to test the necessity of KIF22 motor activity for spindle length maintenance (Tokai-Nishizumi et al., 2005). The phenotypes observed in cells expressing KIF22-GFP T134D or KIF22-GFP T134A are not the same as those observed in cells expressing KIF22-GFP T463D, suggesting that phosphoregulation of T134 is not involved in the inactivation of KIF22.

T158 is located in α2b, the same region of the α2 helix containing amino acids P148 and R149, which are mutated in patients with SEMDJL2 **(Figure 9A)**. Localization of KIF22 to chromosomes is not disrupted by phosphomimetic (T158D) or phosphonull (T158A) mutations at this site. To assess the activity of KIF22-GFP T158D and KIF22-GFP T158A, relative polar ejection forces were measured in monopolar spindles **(Figure 9B)**. In the presence of endogenous KIF22, expression of neither KIF22-GFP T158D nor KIF22-GFP T158A disrupted the generation of polar ejection forces **(Figure 9C)**. In cells depleted of endogenous KIF22, expression of KIF22-GFP, KIF22-GFP T158D, or KIF22-GFP T158A was sufficient to rescue polar ejection force generation **(Figure 9D)**, indicating that KIF22 with mutations at T158 is active in prometaphase and capable of generating polar ejection forces.

To test the effects of phosphomimetic and phosphonull mutations at T158 in anaphase, distances between separating chromosome masses in cells expressing KIF22-GFP, KIF22-GFP T158D, or KIF22-GFP T158A were measured. Expression of KIF22-GFP T158D caused chromosome recongression, while expression of KIF22-GFP T158A did not affect chromosome movements in anaphase **(Figure 9E, 9F)**. The distance between separating chromosome masses

826 7 minutes after anaphase onset was reduced in cells expressing KIF22-GFP T158D (median 6.4
827 μm) compared to cells expressing KIF22-GFP (12.4 μm) or KIF22-GFP T158A (13.6 μm) **(Figure**
828 **9G)**. Mimicking phosphorylation of T158 also affected daughter cell nuclear morphology. Nuclear
829 solidity was reduced in cells expressing KIF22-GFP T158D **(Figure 9H)**, and correspondingly the
830 percentage of cells with abnormally shaped nuclei, designated as a solidity value lower than the
831 5th percentile solidity of control cells expressing GFP, was increased in cells expressing KIF22-
832 GFP T158D in the presence (36%) or absence (32%) of endogenous KIF22 **(Figure 9I)**.
833 Expression of KIF22-GFP (10%) or KIF22-GFP T158A (11%) in the presence of endogenous
834 KIF22 also resulted in a small increase in the percentage of cells with abnormally shaped nuclei
835 compared to control cells expressing GFP (5%). The expression of KIF22-GFP T158D
836 phenocopies the expression of KIF22-GFP T463D or KIF22-GFP with pathogenic mutations,
837 suggesting that dephosphorylation of T158 contributes to KIF22 inactivation in anaphase.

Figure 9

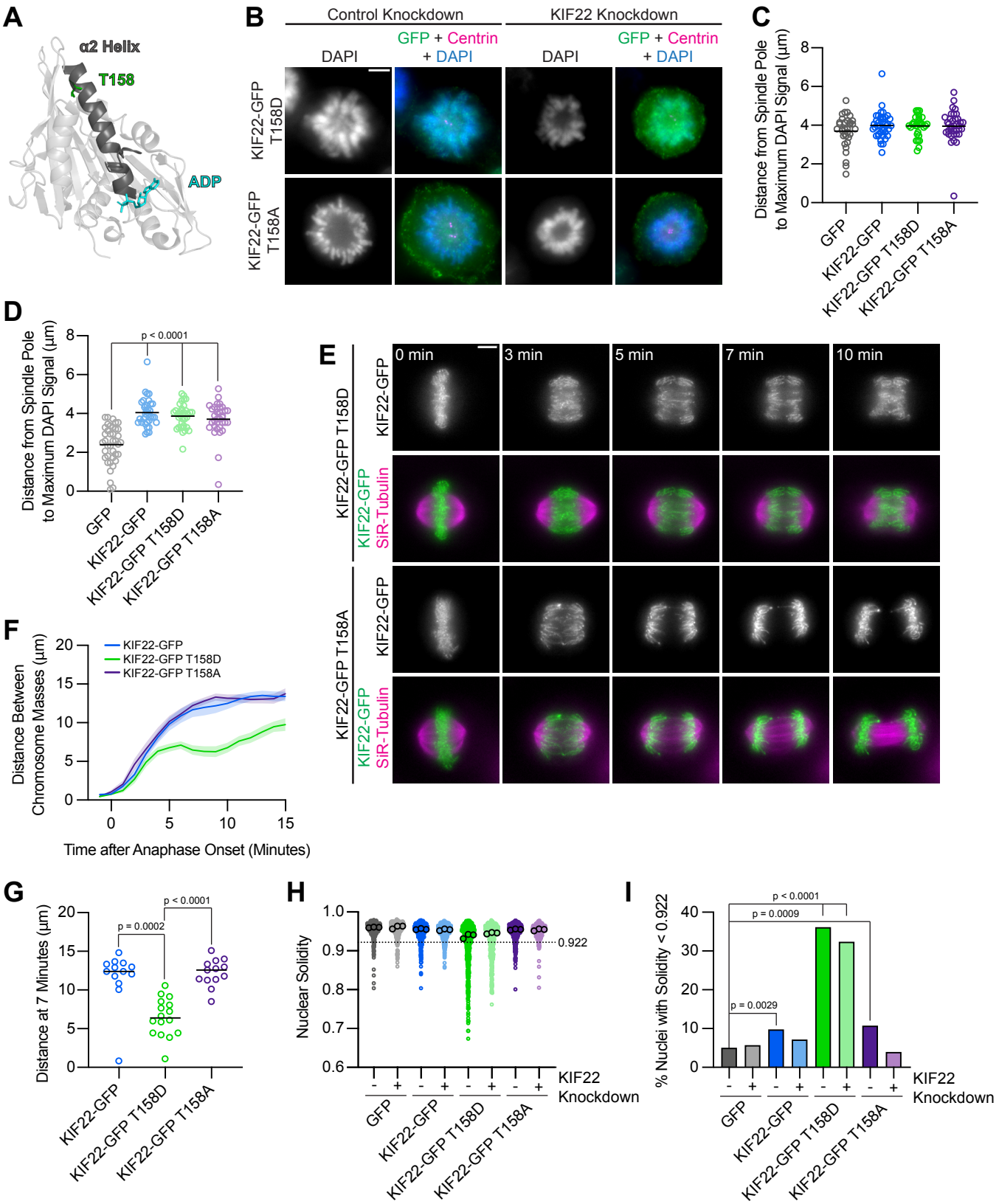

838 **Figure 9: Mimicking phosphorylation of T158 in the motor domain affects KIF22**
839 **inactivation.**
840 **A)** Location of amino acid T158 in the α2 helix of the KIF22 motor domain (PDB 6NJE). **(B)**
841 Immunofluorescence images of monopolar HeLa-Kyoto cells. KIF22-GFP was visualized using
842 an anti-GFP antibody. Fixed approximately 2-3 hours after treatment with monastrol and 24 hours
843 after siRNA transfection and treatment with doxycycline to induce expression. Scale bar 5 μm.
844 Images are representative of 3 or more experiments. **(C)** Distance from the spindle pole to the
845 maximum DAPI signal, a measure of relative polar ejection force level, in HeLa-Kyoto cell lines
846 expressing KIF22-GFP with phosphomimetic and phosphonull mutations at T158. 33 GFP, 40
847 KIF22-GFP, 31 KIF22-GFP T158D, and 36 KIF22-GFP T158A cells from 3 experiments. **(D)**
848 Distance from the spindle pole to the maximum DAPI signal in cells depleted of endogenous
849 KIF22 and expressing KIF22-GFP with phosphomimetic and phosphonull mutations at T158. 39
850 GFP, 35 KIF22-GFP, 34 KIF22-GFP T158D, and 34 KIF22-GFP T158A cells from 3 experiments.
851 For C-D, bars indicate means. p values from Brown-Forsythe and Welch ANOVA with Dunnett's
852 T3 multiple comparisons test. p values are greater than 0.05 for comparisons without a marked p
853 value. **(E)** Time-lapse images of dividing HeLa-Kyoto cells. Cells expressing KIF22-GFP T158D
854 exhibit recongression of the chromosomes during anaphase. Times indicate minutes after
855 anaphase onset. Images are maximum intensity projections in z through the entirety of the
856 spindle. Imaged approximately 18 hours after treatment with doxycycline to induce expression.
857 Scale bar 5 μm. Images are representative of 3 or more experiments. **(F)** Distance between
858 separating chromosome masses throughout anaphase in HeLa-Kyoto cells. Lines represent the
859 mean and the shaded area denotes SEM. 13 KIF22-GFP, 16 KIF22-GFP T158D, and 13 KIF22-
860 GFP T158A cells from 5 experiments. **(G)** Distance between separating chromosome masses 7
861 minutes after anaphase onset. Bars indicate medians. p values from Kruskal-Wallis test. p values
862 are greater than 0.05 for comparisons without a marked p value. 13 KIF22-GFP, 16 KIF22-GFP
863 T158D, and 13 KIF22-GFP T158A cells from 5 experiments. **(H)** Measured solidity of nuclei in
864 HeLa-Kyoto cell lines. Small circles represent the solidity of individual nuclei, and large circles
865 with black outlines indicate the median of each experiment. A dashed line marks a solidity value
866 of 0.922, the fifth percentile of solidity for control cells transfected with control siRNA and
867 expressing GFP. **(I)** Percentage of nuclei with abnormal shape, indicated by a solidity value less
868 than 0.922, the fifth percentile of control (control knockdown, GFP expression) cell solidity. A chi-
869 square test of all data produced a p value < 0.0001. Plotted p values are from pairwise post-hoc
870 chi-square tests comparing control (control knockdown, GFP expression) cells to each other

871 condition. Applying the Bonferroni correction for multiple comparisons, a p value of less than
872 0.00714 was considered significant. p values are greater than 0.00714 for comparisons without a
873 marked p value. Data in (H) and (I) represent 514 GFP control knockdown, 418 GFP KIF22
874 knockdown, 613 KIF22-GFP control knockdown, 584 KIF22-GFP KIF22 knockdown, 644 KIF22-
875 GFP T158D control knockdown, 432 KIF22-GFP T158D KIF22 knockdown, 477 KIF22-GFP
876 T158A control knockdown, and 427 KIF22-GFP T158A KIF22 knockdown cells from 3
877 experiments.

Supplemental Figure 6

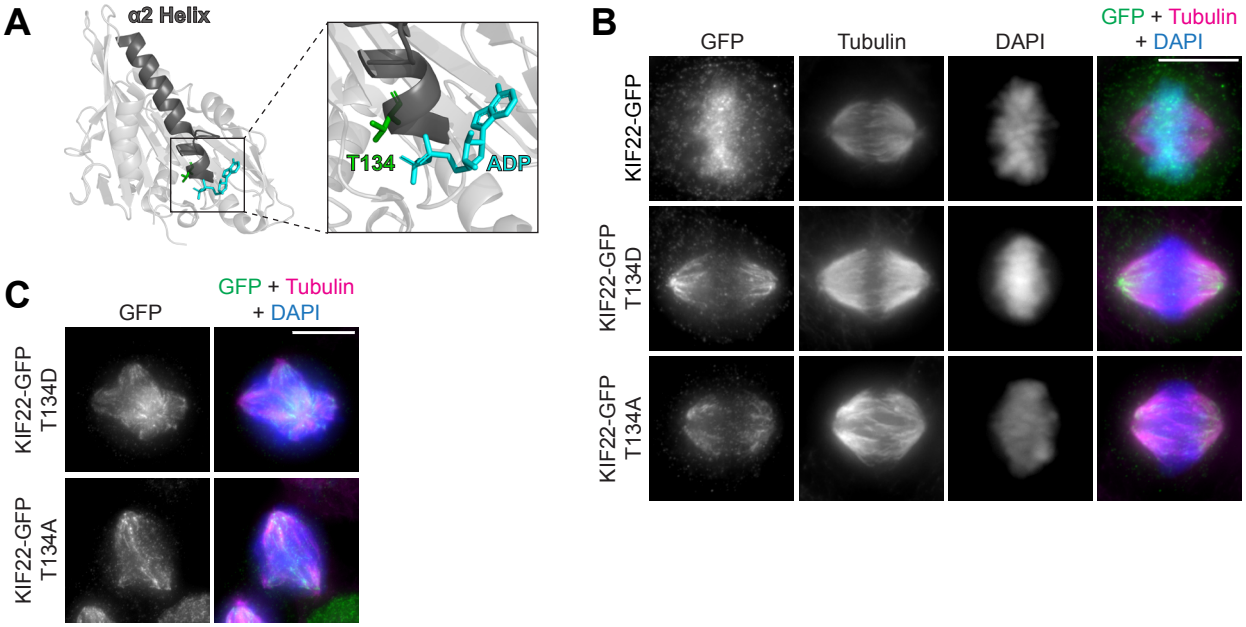

878 **Supplemental Figure 6: Mimicking phosphoregulation of T134 disrupts KIF22 localization.**
879 **(A)** Location of amino acid T134 in the α2 helix of the KIF22 motor domain (PDB 6NJE). **(B)**
880 Immunofluorescence images of HeLa-Kyoto cells expressing KIF22-GFP constructs in
881 metaphase. KIF22-GFP was visualized using an anti-GFP antibody. Images are maximum
882 intensity projections in z. Fixed approximately 24 hours after treatment with doxycycline to induce
883 expression. Scale bar 10 μm. **(C)** Immunofluorescence images of multipolar HeLa-Kyoto cells
884 expressing KIF22-GFP T134D or KIF22-GFP T134A. Images are maximum intensity projections
885 in z. Fixed approximately 24 hours after treatment with doxycycline to induce expression. Scale
886 bar 10 μm.

Figure 10

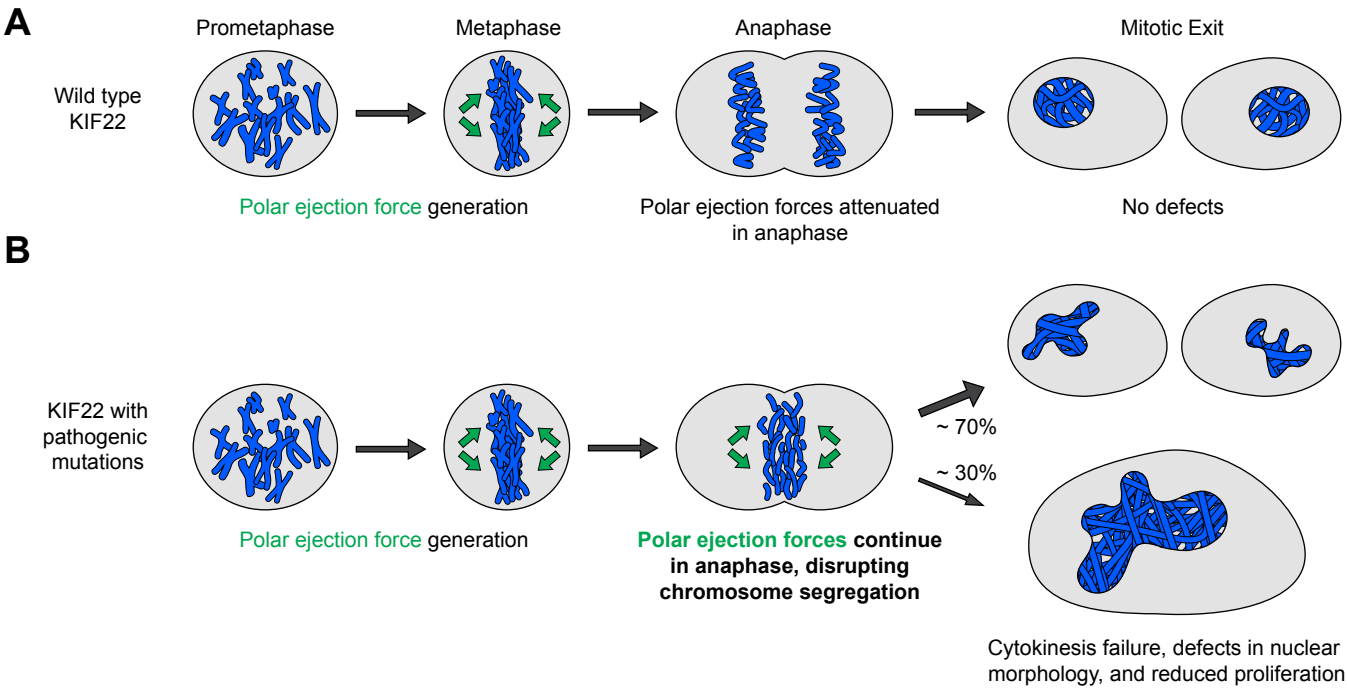

887 **Figure 10: Pathogenic mutations disrupt the anaphase, but not prometaphase, function of**
888 **KIF22.**
889 **(A)** Wild type KIF22 generates polar ejection forces to contribute to chromosome congression
890 and alignment in prometaphase. In anaphase, KIF22 inactivation results in the attenuation of polar
891 ejection forces (green arrows), allowing chromosomes to segregate toward the poles. Daughter
892 cells form regularly shaped nuclei and continue to proliferate. **(B)** In cells expressing KIF22 with
893 pathogenic (P148L, P148S, R149L, R149Q, V475G) or phosphomimetic (T158D, T463D)
894 mutations, prometaphase proceeds as in cells expressing wild type motor. Mutant KIF22 is
895 capable of polar ejection force generation. In anaphase, KIF22 fails to inactivate, resulting in
896 continued generation of polar ejection forces, which disrupts anaphase chromosome segregation.
897 Daughter cells exhibit nuclear morphology defects. In about 30% of cells expressing KIF22-GFP
898 R149Q or KIF22-GFP V475G, cytokinesis fails, and proliferation rates are reduced.

DISCUSSION

We have determined that pathogenic mutations in KIF22 disrupt anaphase chromosome segregation, causing chromosome recongression, nuclear morphology defects, reduced proliferation, and, in a subset of cells, cytokinesis failure. Wild type KIF22 is inactivated in anaphase (Soeda et al., 2016), resulting in an attenuation of polar ejection forces, which allows chromosomes to move towards the spindle poles **(Figure 9A)**. The phenotypes we observe in cells expressing KIF22-GFP with pathogenic mutations are consistent with KIF22 remaining active in anaphase **(Figure 9B)**. Polar ejection forces could cause recongression by continuing to push chromosomes away from the spindle poles during anaphase A and disrupting spindle elongation during anaphase B. These forces result in aberrant positioning of chromosomes during telophase and cytokinesis, which could cause the nuclear morphology defects and cytokinesis failure we observe in cells expressing mutant KIF22-GFP. Consistent with this model, mimicking phosphorylation of T463 to prevent KIF22 inactivation in anaphase phenocopies the effects of pathogenic mutations. Thus, we conclude that pathogenic mutations result in a gain of KIF22 function, which aligns with findings that KIF22 mutations are dominant in heterozygous patients (Boyden et al., 2011; Min et al., 2011; Tüysüz et al., 2014). The effects of pathogenic mutations on chromosome movements in anaphase are consistent with observations of chromosome recongression in cells with altered CDK1 activity (Su et al., 2016; Wolf et al., 2006) or altered tail structure (Soeda et al., 2016). Our work additionally demonstrates the involvement of the motor domain α2 helix in this process and the consequences of recongression on cytokinesis, daughter cell nuclear morphology, and proliferation.

Mutations in both the motor domain (P148L, P148S, R149L, and R149Q) and the coiled-coil domain (V475G) of KIF22 disrupt chromosome segregation in a manner consistent with a failure of KIF22 inactivation in anaphase. Additionally, mimicking phosphorylation of T158 in the motor domain or T463 in the tail also disrupts chromosome segregation. These findings demonstrate that the motor domain α2 helix participates in the process of KIF22 inactivation, adding to studies that demonstrate that deletion of the tail microtubule binding domain and deletion or disruption of the coiled-coil domain prevent the inactivation of KIF22 in anaphase (Soeda et al., 2016).

The physical mechanism of KIF22 inactivation is unknown, and our results can be interpreted in the context of several models, which are not mutually exclusive. Previous work has proposed that the tail of KIF22 may interact with microtubules to suspend polar ejection force generation (Soeda et al., 2016). In this framework, the mutation in the tail of KIF22 (V745G) could disrupt anaphase chromosome segregation by altering this interaction with microtubules. Whether

or how the α2 helix could contribute to this mechanism is less clear. The α2 helix faces away from the surface of the microtubule, and we would not predict that mutations in this structure would directly alter the association of the motor domain with the microtubule. It is possible that this region of the motor domain could facilitate or strengthen an interaction between the tail and the microtubule surface indirectly.

Alternatively, given that mutations in the tail and motor domain of KIF22 both disrupt chromosome segregation, the tail and motor domain may interact to inactivate the motor. Head-tail autoinhibition is a known regulatory mechanism of other members of the kinesin superfamily (Blasius et al., 2021; Coy, Hancock, Wagenbach, & Howard, 1999; Espeut et al., 2008; Friedman & Vale, 1999; Hammond, Blasius, Soppina, Cai, & Verhey, 2010; Hammond et al., 2009; Imanishi, Endres, Gennerich, & Vale, 2006; Ren et al., 2018; Verhey & Hammond, 2009; Verhey et al., 1998), and disruption of autoinhibition can be a mechanism of disease pathogenesis (Asselin et al., 2020; Bianchi et al., 2016; Blasius et al., 2021; Cheng et al., 2014; Pant et al., 2022; van der Vaart et al., 2013). Mutations in either the tail or motor domain could disrupt this interaction, preventing KIF22 inactivation in anaphase. Dephosphorylation of both T463 in the tail and T158 in the motor domain could facilitate this interaction.

Rather than physically interacting with the motor domain, it is also possible that structural changes in the tail of KIF22 could have allosteric effects on the motor domain. An allosteric mechanism by which conformational changes are propagated down the stalk to the motor domain has recently been proposed to contribute to the inactivation of kinesin-1 motors by kinesin light chain, which binds the tail (Chiba, Ori-McKenney, Niwa, & McKenney, 2021). KIF22 inactivation may be caused by altered motor domain mechanochemistry, which changes in the tail could affect allosterically and modification of α2 could affect directly. This could explain the effect of tail and motor domain mutations, as well as the effects of mimicking tail and motor domain phosphorylation, on KIF22 activity.

An additional consideration is that pathogenic mutations may affect the inactivation of KIF22 in anaphase by altering phosphoregulation of KIF22 activity. If mutations prevented the dephosphorylation of T158 and T463 in anaphase this could cause anaphase recongression. However, addition of a phosphonull T463A mutation to KIF22 with coiled-coil or microtubule binding domain deletions does not rescue anaphase chromosome recongression defects (Soeda et al., 2016), suggesting that the role of the KIF22 tail in motor inactivation is not only to facilitate dephosphorylation of T463. Future studies using structural approaches will be required to distinguish between these possible mechanisms.

The regulation of the motor domain α2 helix in KIF22 inactivation may inform our understanding of additional kinesin motors, as amino acids P148 and R149 are conserved in a number of members of the kinesin superfamily **(Figure 1D)**. Similarly, phosphorylation or acetylation of amino acids in the α2 helix has been reported for members of the kinesin-3 (KIF13A S134) (Dephoure et al., 2008), kinesin-5 (KIF11 Y125, K146) (Bickel et al., 2017; Choudhary et al., 2009), kinesin-6 (KIF20B S182, KIF23 S125) (Hegemann et al., 2011; Sharma et al., 2014; Shiromizu et al., 2013), and kinesin-14 (KIFC3 S557) (Sharma et al., 2014) families. Phosphorylation of Y125 (Bickel et al., 2017) and acetylation of K146 (Muretta et al., 2018) in KIF11 (Eg5) have been shown to modulate motor activity, and the functions of the remaining reported post-translation modifications in the α2 helix are yet to be characterized. Acetylation of KIF11 at K146 increases the stall force of the motor and slows anaphase spindle pole separation (Muretta et al., 2018). This post-translational modification represents a mechanism by which the activity of KIF11 could be regulated at the metaphase to anaphase transition to generate sliding forces for spindle assembly in prometaphase and control spindle pole separation in anaphase, analogous to how post-translational modifications of KIF22 regulate motor activity to ensure both chromosome congression and alignment in prometaphase and chromosome segregation in anaphase.

While chromosomes in some cells, particularly those expressing KIF22-GFP at high levels, completely failed to segregate and decondensed in the center of the spindle, most cells demonstrated chromosome recongression wherein poleward motion of chromosomes begins, but then chromosomes switch direction and move anti-poleward. These dynamics may be due to differences in microtubule density closer to the poles compared to the center of the spindle. This model is consistent with work demonstrating that in monopolar spindles, poleward movement of chromosomes is limited by chromosomes reaching a threshold density of microtubules at which polar ejection forces are sufficient to cause chromosomes to switch to anti-poleward movement (Cassimeris, Rieder, & Salmon, 1994). We observed that chromosomes on the periphery of the spindle remain closer to the poles while central chromosomes are pushed further away from the poles during recongression in cells expressing KIF22-GFP with pathogenic mutations. This could also be explained by the central chromosomes encountering a higher density of microtubules, and KIF22 bound to these chromosomes therefore generating higher levels of polar ejection forces. In addition, this mechanism is consistent with observations that oscillations of peripheral chromosomes are reduced compared to chromosomes at the center of the spindle (Cameron et al., 2006; Cimini, Cameron, & Salmon, 2004; Civelekoglu-Scholey et al., 2013; Stumpff, Dassow,

Wagenbach, Asbury, & Wordeman, 2008), which could also be explained by reduced peripheral microtubule density limiting peripheral polar ejection force generation.

Our assessment of the relative trajectories of chromosomes, centromeres, and spindle poles offers insight into the relative magnitudes of polar ejection forces and other anaphase forces. Expression of KIF22-GFP with pathogenic mutations did not alter the distance between centromeres and spindle poles, indicating that while anaphase polar ejection forces altered the position of chromosome arms within the spindle, these forces were not sufficient to prevent the shortening of k-fibers. However, the expression of mutant KIF22-GFP did alter the movements of the spindle poles, allowing assessment of the relative magnitude of polar ejection forces compared to the forces generated by the sliding of antiparallel spindle microtubules to separate the spindle poles in anaphase (Brust-Mascher, Civelekoglu-Scholey, Kwon, Mogilner, & Scholey, 2004; Fu et al., 2009; Nislow, Lombillo, Kuriyama, & McIntosh, 1992; Sawin, LeGuellec, Philippe, & Mitchison, 1992; Straight, Sedat, & Murray, 1998; Tanenbaum et al., 2009; van Heesbeen, Tanenbaum, & Medema, 2014; Vukušić, Buđa, & Tolić, 2019; Vukušić, Ponjavić, Buđa, Risteski, & Tolić, 2021). In cells expressing mutant KIF22-GFP, spindle pole separation stalled, and poles moved closer to one another during anaphase chromosome recongression. This suggests that the polar ejection forces collectively generated by mutant KIF22 motors are of greater magnitude than the forces sliding the spindle poles apart during anaphase B. Although it is important to note that this phenotype was observed with moderate overexpression of mutant KIF22, the observed effects on spindle pole separation underscore the importance of KIF22 inactivation, and imply that reducing polar ejection forces is required for both anaphase A and anaphase B. This force balance may differ between cell types, as tail domain deletions that alter chromosome movements do not disrupt anaphase B in mouse oocyte meiosis (Soeda et al., 2016).

Patients with mutations in KIF22 exhibit defects in skeletal development. The pathology observed in the patient heterozygous for the V475G mutation differs from those seen in SEMDJL2 patients with motor domain mutations **(Figure 1E, 1F)** (Boyden et al., 2011; Min et al., 2011; Tüysüz et al., 2014). However, a meaningful comparison of pathologies between patients is limited both by the fact that only a single patient with a mutation in the tail of KIF22 has been identified, and by the considerable variation in clinical presentation between patients with motor domain mutations, even between patients with the same point mutation (Boyden et al., 2011; Min et al., 2011; Tüysüz et al., 2014). The defects in chromosome segregation we observed in cells expressing mutant KIF22-GFP may contribute to skeletal developmental pathogenesis. Mutations could cause reduced proliferation of growth plate chondrocytes, which in turn could limit bone growth. Disrupting cytokinesis in the growth plate causes shorter bones and stature in mice (Gan

et al., 2019), and mutations in KIF22 could affect development via this mechanism. The presence of pathologies in other cartilaginous tissues, including the larynx and trachea, in patients with mutations in the motor domain of KIF22 (Boyden et al., 2011) is also consistent with a disease etiology based in aberrant chondrocyte proliferation. Defects in mitosis could result in tissue-specific patient pathology based on differences in force balance within anaphase spindles in different cell types arising from different expression or activity levels of mitotic force generators or regulators. Growth plate chondrocytes, particularly, are organized into columns and must divide under geometric constraints (Dodds, 1930), which could increase sensitivity to anaphase force imbalances. Additionally, we cannot exclude the possibility that these mutations may affect the function of interphase cells, which could affect development via a mechanism independent from the effects of the mutations on mitosis. Future work will be required to distinguish among these possible explanations.

MATERIALS AND METHODS

Patient assessment

Clinical exome sequencing was performed by the Department of Laboratory Medicine and Pathology at Mayo Clinic in Rochester, Minnesota, USA as previously described (Cousin et al., 2019). Carbohydrate deficient transferrin testing for congenital disorders of glycosylation was performed at Mayo Clinic Laboratories, Rochester, Minnesota, USA (Lefeber, Morava, & Jaeken, 2011).

Cell culture

HeLa-Kyoto and RPE-1 cell lines were grown in Minimum Essential Media α (Gibco #12561-056) supplemented with 10% fetal bovine serum (Gibco #16000-044) at 37°C with 5% CO_2. Cell lines were validated by short tandem repeat (STR) DNA typing using the Promega GenePrint 10 System according to the manufacturer's instructions (Promega #B9510). Cells were cryopreserved in Recovery Cell Culture Freezing Medium (Gibco #12648-010). HeLa-Kyoto and RPE-1 acceptor cell lines for recombination (both gifts from Ryoma Ohi, University of Michigan) were maintained in media supplemented with 10 μg/mL blasticidin (Thermo Fisher Scientific #R21001).

Transfection

siRNA transfection was performed using Lipofectamine RNAiMax Transfection Reagent (Thermo Fisher Scientific #13778150) in Opti-MEM Reduced Serum Media (Gibco #31985-062).

KIF22 was targeted for siRNA-mediated depletion using a Silencer Validated siRNA (Ambion #AM51331, sense sequence GCUGCUCUCUAGAGAUUGCTT). Control cells were transfected with Silencer Negative Control siRNA #2 (Ambion #AM4613). DNA transfections were performed using Lipofectamine LTX (Thermo Fisher Scientific #15338100) in Opti-MEM Reduced Serum Media (Gibco #31985-062).

Plasmids

Plasmids related to the generation of inducible cell lines are described in Table 1. A C-terminally tagged KIF22-GFP plasmid was constructed by adding EcoRI and KpnI sites to the KIF22 open reading frame (from pJS2161 (Stumpff et al., 2012)), performing a restriction digest, and ligating the products into a digested pEGFP-N2 vector (Clontech) (pAT4206). Site-directed mutagenesis was performed to add silent mutations for siRNA resistance (pAT4226). The open reading frame from pAT4226 and the pEM791 vector (Khandelia, Yap, & Makeyev, 2011) were amplified and combined using Gibson Assembly (New England BioLabs) to generate a plasmid for recombination-mediated construction of inducible cell lines (pAT4250). Site-directed mutagenesis was performed on pAT4250 to generate plasmids encoding KIF22-GFP P148L, P148S, R149L, R149Q, V475G, T463D, T463A, T134D, T158D, and T158A for recombination. A plasmid encoding KIF22-GFP T134A for recombination was generated using Gibson Assembly of a synthesized DNA fragment (Thermo Fisher Scientific) and pAT4250. See Table 1 for primer sequences.

The mCh-CAAX plasmid was a gift from Alan Howe (University of Vermont). The mCh-NLS plasmid was generated by Michael Davidson and obtained from Addgene (mCh-Nucleus-7, #55110). The pericentrin-RFP plasmid (Gillingham & Munro, 2000) was a gift from Sean Munro (MRC Laboratory of Molecular Biology). The CENPB-mCh plasmid (D. Liu et al., 2010) was generated by Michael Lampson and obtained from Addgene (#45219).

Generation of inducible cell lines

Inducible cell lines were generated using recombination-mediated cassette exchange as previously described (Khandelia et al., 2011). Briefly, plasmids (see Table 1) encoding siRNA-resistant KIF22-GFP constructs were cotransfected with a plasmid encoding nuclear-localized Cre recombinase (pEM784) into HeLa-Kyoto (Sturgill, Norris, Guo, & Ohi, 2016) or RPE-1 acceptor cells using Lipofectamine LTX transfection (Thermo Fisher Scientific #15338100). For HeLa-Kyoto cell lines, 24 hours after transfection cells were treated with 1 μg/mL puromycin (Thermo Fisher Scientific #A11139-03) for 48 hours, then 2 μg/mL puromycin for 48 hours for

more stringent selection, and finally 1 μg/mL puromycin until puromycin-sensitive cells were eliminated. Selection of RPE-1 cells was accomplished via treatment with 5 μg/mL puromycin for 48 hours beginning 24 hours after transfection, then 10 μg/mL puromycin for 48 hours, and finally 5 μg/mL puromycin until puromycin-sensitive cells were eliminated. Inducible cell lines were maintained in puromycin (HeLa-Kyoto 1 μg/mL, RPE-1 5 μg/mL) for continued selection. To confirm the sequence of inserted DNA in the selected cell populations, genomic DNA was extracted using the QIAmp DNA Blood Mini Kit (Qiagen #51106) and subjected to sequencing (Eurofins). Expression of inserted DNA sequences was induced via treatment with 2 μg/mL doxycycline (Thermo Fisher Scientific #BP26531).

Immunofluorescence

For fixed cell imaging, cells were grown on 12 mm glass coverslips in 24-well plates. Cells were fixed in 1% paraformaldehyde in ice-cold methanol for 10 minutes on ice. Cells were blocked for 1 hour using 20% goat serum (Gibco #16210-064) in antibody dilution buffer (AbDil, 1% bovine serum albumin (Sigma Aldrich #B4287), 0.1% Triton X-100 (Sigma Aldrich #93443), 0.02% sodium azide (Fisher Scientific #BP9221) in TBS) and incubated with the following primary antibodies for one hour at room temperature: mouse anti-α-tubulin (DM1α) 1:500 (Millipore Sigma #T6199), rat anti-tubulin clone YL1/2 1:1500 (Millipore Sigma #MAB1864), rabbit anti-KIF22 1:500 (GeneTex #GTX112357), mouse anti-centrin 1:500 (Millipore Sigma #04-1624), or rabbit anti-GFP 1:1000 (Invitrogen #A11121). Cells were incubated with secondary antibodies conjugated to AlexaFluor 488, 594, or 647 (Invitrogen Molecular Probes #A11034, A11037, A21245, A11029, A11032, A21236, A11007) for one hour at room temperature. All incubations were performed on an orbital shaker. Coverslips were mounted on slides using Prolong Gold mounting medium with DAPI (Invitrogen Molecular Probes #P36935).

Microscopy

Images were acquired using a Nikon Ti-E or Ti-2E inverted microscope driven by NIS Elements software (Nikon Instruments). Images were captured using a Clara cooled charge-coupled device (CCD) camera (Andor) or Prime BSI scientific complementary metal-oxide-semiconductor (sCMOS) camera (Teledyne Photometrics) with a Spectra-X light engine (Lumencore). Samples were imaged using Nikon objectives Plan Apo 40X 0.95 numerical aperture (NA), Plan Apo λ 60X 1.42 NA, and APO 100X 1.49 NA. For live imaging, cells were imaged in CO_2-independent media (Gibco #18045-088) supplemented with 10% fetal bovine

serum (Gibco #16000-044) in a 37º C environmental chamber. Images were processed and analyzed using Image J/FIJI (Schindelin et al., 2012; Schneider, Rasband, & Eliceiri, 2012).

KIF22-GFP expression level quantitation

HeLa-Kyoto or RPE-1 cells were treated with 2 μg/mL doxycycline to induce expression and transfected with control or KIF22 siRNA approximately 24 hours prior to fixation. Metaphase cells were imaged for measurement of KIF22 expression levels. Measurements of KIF22 immunofluorescence intensity were made in a background region of interest (ROI) containing no cells and an ROI representing the chromosomes, identified by thresholding DAPI signal. The mean background subtracted KIF22 signal on the chromosomes was calculated by subtracting the product of the mean background intensity and the chromosome ROI area from the chromosome ROI integrated density and dividing by the area of the chromosome ROI. KIF22 intensities were normalized to the mean KIF22 intensity in control cells (control knockdown, uninduced) in each experimental replicate.

Metaphase chromosome spreads

RPE-1 cells were grown in 60 mm dishes for approximately 24 hours. Media was exchanged to fresh growth media for 2 hours to promote mitosis. Cells were arrested in 0.02 μg/mL colcemid (Gibco KaryoMAX #15212012) for three hours at 37°C, then trypsinized, pelleted, and gently re-suspended in 500 μL media. 5 mL 0.56% KCl hypotonic solution was added dropwise to the cell suspension, which was then incubated for 15 minutes in a 37°C water bath. Cells were pelleted, gently resuspended, and fixed via the addition of 1 mL ice-cold 3:1 methanol:glacial acetic acid. Cells were pelleted and resuspended in fixative an additional three times, then stored at -20°C. Metaphase chromosome spreads were prepared by humidifying the surface of glass slides by exposing them to the steam above a 50°C water bath, placing the slides at an angle relative to the work surface, and dropping approximately 100 μL of ice-cold cell suspension onto the slide from a height of approximately one foot. Slides were dried on a hot plate, then covered with Prolong Gold mounting medium with DAPI (Invitrogen Molecular Probes #P36935) and sealed.

Fluorescence recovery after photobleaching

HeLa-Kyoto cells were seeded in glass-bottom 35 mm dishes (Greiner Bio-One #627975 and #627965) and treated with 2 μg/mL doxycycline to induce expression 18-24 hours before

imaging. Cells were imaged at 5 second intervals for 25 seconds before bleaching, photobleached using a point-focused 405 nm laser, and imaged at 20 second intervals for 10 minutes after bleaching. Fluorescence intensities in bleached, unbleached, and background regions of each frame were measured using a circular ROI, area 0.865 μm^2. For interphase and metaphase cells, unbleached measurements were made on the opposite side of the nucleus or chromosome mass as the bleached measurements. For anaphase cells, one segregating chromosome mass was bleached, and unbleached measurements were made on the opposite chromosome mass. Background intensities, measured in cell-free area, were subtracted from bleached and unbleached intensities. Background-subtracted intensities were normalized to the intensity of the first frame imaged.

Polar ejection force assay

HeLa-Kyoto cells were treated with 2 μg/mL doxycycline to induce expression and transfected with control or KIF22 siRNA approximately 24 hours prior to fixation. Cells were arrested in 100 μM monastrol (Selleckchem #S8439) for 2-3 hours before fixation. Monopolar mitotic cells oriented perpendicular to the coverslip were imaged at the focal plane of the spindle pole for polar ejection force measurements. A circular ROI with a 12.5 μm radius was centered around the spindle pole of each cell, and the radial profile of DAPI signal intensity at distances from the pole was measured (Radial Profile Plot plugin, https://imagej.nih.gov/ij/plugins/radial-profile.html). The distance from the pole to the maximum DAPI signal was calculated for each cell as a measure of relative polar ejection forces (Thompson, Vandal, & Stumpff, 2022).

Analyses of anaphase chromosome segregation

HeLa-Kyoto or RPE-1 cells were treated with 2 μg/mL doxycycline to induce expression approximately 18 hours before imaging. For HeLa-Kyoto cells, media was exchanged to CO_2-indpendent media containing 2 μg/mL doxycycline and 100 nM SiR-Tubulin (Spirochrome #SC002) approximately 1-1.5 hours before imaging. For RPE-1 cells, media was exchanged to CO_2-indpendent media containing 2 μg/mL doxycycline, 20-100 nM SiR-Tubulin (Spirochrome #SC002), and 10 μM verapamil (Spirochrome #SCV01) approximately 1.5-3 hours before imaging. Cells were imaged at 1 minute time intervals. Distances between segregating chromosome masses were measured by plotting the KIF22-GFP signal intensity along a line drawn through both spindle poles (macro available at https://github.com/StumpffLab/Image-Analysis). This data set was split at the center distance to generate two plots, each representing

one half-spindle/segregating chromosome mass. The distance between the maximum of each intensity plot was calculated using MATLAB (Mathworks, Version R2018a) (script available at https://github.com/StumpffLab/Image-Analysis). To assess the broadness of segregating chromosome masses in cells expressing KIF22-GFP T463A, a Gaussian curve was fit to the same intensity plots and the full width at half maximum was calculated in MATLAB.

To measure the movements of spindle poles and kinetochores in anaphase, HeLa-Kyoto cells were seeded in glass-bottom 24-well plates (Cellvis #P24-1.5H-N) and cotransfected with PCM-RFP and mCh-CENPB using Lipofectamine LTX (Thermo Fisher Scientific #15338100) approximately 24 hours before imaging. Cells were treated with 2 μg/mL doxycycline to induce expression approximately 12-18 hours before imaging. Cells were imaged at 20 second time intervals. To more clearly visualize spindle poles and kinetochores, images of PCM-RFP and mCh-CENPB signal were background subtracted by duplicating each frame, applying a gaussian blur (sigma 30 pixels), and subtracting this blurred image from the original. For each frame, a line was drawn between spindle poles (PCM-RFP signal) to measure the distance between them, and the intensity of KIF22-GFP and mCh-CENPB along this line was plotted. These data sets were split at the center distance to generate two plots, and the distance between plot maxima and the distance from maxima to the spindle poles were calculated using MATLAB (scripts available at https://github.com/StumpffLab/Image-Analysis).

Assessment of cytokinesis failure

To visualize cell boundaries, HeLa-Kyoto cells were transfected with mCh-CAAX using Lipofectamine LTX approximately 24-32 hours before imaging and treated with 2 μg/mL doxycycline approximately 8 hours before imaging. Cells were imaged at 3-minute intervals. Cells were scored as failing cytokinesis if the product of mitosis was a single cell with a single boundary of mCh-CAAX signal.

Nuclear morphology quantification

HeLa-Kyoto or RPE-1 cells were treated with 2 μg/mL doxycycline to induce expression approximately 24 hours before fixation. Nuclear solidity was measured for each interphase nucleus in each imaged field. The 5th percentile of solidity for control cells (transfected with control siRNA and expressing GFP) was used as a threshold below which nuclear solidity was considered abnormal.

To assess the ability of nuclei to retain nuclear-localized proteins, cells were transfected with mCh-NLS using Lipofectamine LTX approximately 24-32 hours before imaging and treated

with 2 μg/mL doxycycline approximately 8 hours before imaging. Cells were imaged at 3-minute intervals during and after division, and the presence of mCh-NLS signal in all nuclear structures (KIF22-GFP positive regions) was assessed.

Assessment of spindle dependence of nuclear morphology defects

To assess whether nuclear morphology defects caused by KIF22 depend on force generation within the mitotic spindle, cells were treated with 2 μg/mL doxycycline approximately 8 hours before imaging, SPY595-DNA (1X per manufacturer's instructions) (Spirochrome #SC301) approximately 1.5-2 hours before imaging, and 500 nM nocodazole (Selleckchem #S2775) and 900 nM reversine (Cayman Chemical #10004412) approximately 0.5-1 hour before imaging. Cells were imaged at 5-minute intervals. Nuclear solidity was measured 15 minutes before chromosome condensation and 100 minutes after chromosome decondensation.

Proliferation assay

HeLa-Kyoto cells were seeded in a 96-well plate and treated with 2 μg/mL doxycycline to induce expression or transfected with KIF22 siRNA approximately eight hours before the first assay timepoint. Automated bright field imaging using a Cytation 5 Cell Imaging Multi-Mode Reader (Biotek) (4X Plan Fluorite 0.13 NA objective (Olympus)) driven by Gen5 software (Biotek) was used to measure cell proliferation (Marquis et al., 2021). Images were collected every 4 hours for 96 hours. Gen5 software was used to process images and count the number of cells in each imaged field. Cell counts were normalized to the cell count in the first image acquired at time 0. Only wells with first frame cell counts between 10,000 and 20,000 were analyzed to account for the effects of cell density. Fold change at 96 hours was calculated by dividing the cell count at 96 hours by the cell count at time 0. Predicted cell counts at 48 hours were calculated using an experimentally determined doubling time of 20.72 hours for the control case where all cells divide ($Cells_T = 2^{(\frac{T}{20.72})}$), the case where nuclear morphology defects limit proliferation and 60% of cells do not divide ($Cells_T = 1.4^{(\frac{T}{20.72})}$), and the case where cytokinesis failure limits proliferation and 30% of cells do not divide ($Cells_T = 1.7^{(\frac{T}{20.72})}$).

Statistical analyses

Statistical tests were performed using GraphPad Prism software (GraphPad Software, Inc.), version 9.2.0. Specific statistical tests and n values for reported data are indicated in the figure legends. All data represent a minimum of three independent experiments.

1267 **Table 1**

Plasmid	Description	Primers (5' to 3', Fw: Forward, Rev: Reverse)	Source
pEM784	nlCre recombinase	NA	Khandelia 2011 PMID 21768390
pEM791	EGFP for recombination	NA	Khandelia 2011 PMID 21768390
pJS2161	GFP-KIF22	NA	Stumpff 2012 PMID 22595673
pAT4206	KIF22-GFP	Fw: TACGTGGAATTCCACCATGGCCGCGGGCGGCTCGA Rev: GTGACTGGTACCTGGAGGCGCCACAGCGCTGGC	This study
pAT4226	KIF22-GFP, siRNA resistant	Fw:pGGGCATGGACAGCTGCTCACTCGAAATCGCTAACTGGAGGA ACCAC Rev:pGTGGTTCCTCCAGTTAGCGATTTCGAGTGAGCAGCTGTCCA TGCCC	This study
pAT4250	KIF22-GFP, siRNA resistant, for recombination	Fragment Fw: CTGGGCACCACCATGGCCGCG Fragment Rev: GCTAGCTCGATTACTTGTACAGCTCGTCCATGCC Vector Fw: GTACAAGTAATCGAGCTAGCATATGGATCCATATAACT Vector Rev: CATGGTGGTGCCCAGTGCCTCACGACC	This study
pAT4251	KIF22-GFP R149Q	Fw: GGGGTGATCCCGCAGGCTCTCATGGAC Rev: GTCCATGAGAGCCTGCGGGATCACCCC	This study
pAT4258	KIF22-GFP V475G	Fw: TGCTAATGAAGACAGGAGAAGAGAAGGACCT Rev: AGGTCCTTCTCTTCTCCTGTCTTCATTAGCA	This study
pAT4260	KIF22-GFP T463D	Fw: CCCCTCTGTTGAGTGACCCAAAGCGAGAGC Rev: GCTCTCGCTTTGGGTCACTCAACAGAGGGG	This study
pAT4261	KIF22-GFP T463A	Fw: CCTCTGTTGAGTGCCCCAAAGCGAG Rev: CTCGCTTTGGGGCACTCAACAGAGG	This study
pAT4264	KIF22-GFP R149L	Fw: GGGTGATCCCGCTGGCTCTCATGGAC Rev: GTCCATGAGAGCCAGCGGGATCACCC	This study
pAT4269	KIF22-GFP P148L	Fw: CCTGGGGTGATCCTGCGGGCTCTCATG Rev: CATGAGAGCCCGCAGGATCACCCCAGG	This study
pAT4270	KIF22-GFP P148S	Fw: CTGGGGTGATCTCGCGGGCTCTCATG Rev: CATGAGAGCCCGCGAGATCACCCCAG	This study
pSS4279	KIF22-GFP T134A	Fragment Fw: AGCTGCTCACTCGAAATCGC Fragment Rev: AGTCTTTCTCGGATTACCAGG Vector Fw: CCTGGTAATCCGAGAAGACT Vector Rev: GCGATTTCGAGTGAGCAGCT	This study
pSS4281	KIF22-GFP T134D	Fw: CAGGAGCTGGGAAGGATCACACAATGCTGGGC Rev: GCCCAGCATTGTGTGATCCTTCCCAGCTCCTG	This study
pNA4285	KIF22-GFP T158A	Fw: AGCTCGCAAGGGAGGAGGGTG Rev: GAGTACCTGGAGGACGTCGA	This study
pNA4284	KIF22-GFP T158D	Fw: CCTCCTGCAGCTCAGGGAGGAGGGTG Rev: CACCCTCCTCCCTGAGCTGCAGGAGG	This study

ACKNOWLEDGEMENTS

This work was supported by NIH F31AR074887 to AFT, NIH R01GM130556 to JKS, NIH R01GM121491 to JKS, and the Ballenger Ventures Fund for Research Excellence. We thank the Mayo Clinic Center for Individualized Medicine (CIM) for supporting this research through the CIM Investigative and Functional Genomics program. We thank Alan Howe for the mCh-CAAX plasmid, and Ryoma Ohi for reagents and acceptor cells for recombination-mediated cassette exchange. We thank Rachel Stadler for technical assistance with data analysis and thank Laura Reinholdt and Matthew Warman for constructive discussions regarding this work.

COMPETING INTERESTS

The authors declare no competing financial interests.

VIDEO LEGENDS

Video 1. Fluorescence recovery after photobleaching of KIF22-GFP.

Fluorescence recovery after photobleaching (FRAP) in HeLa-Kyoto cells expressing KIF22-GFP (top), KIF22-GFP R149Q (middle), or KIF22-GFP V475G (bottom). Cells represent interphase (left), metaphase (middle), or anaphase (right). Bleaching occurred at time zero. Scale bar 10 μm. Cells were imaged at 5 second intervals for 25 seconds before bleaching, photobleached, and imaged at 20 second intervals for 10 minutes after bleaching. Playback at 10 frames per second.

Video 2. Anaphase in HeLa-Kyoto cells.

Anaphase chromosome segregation in HeLa-Kyoto cells expressing KIF22-GFP (left), KIF22-GFP R149Q (middle), or KIF22-GFP V475G (right). Magenta: SiR-Tubulin, green: KIF22-GFP. Times indicate minutes after anaphase onset. Scale bar 5 μm. Cells were imaged at 1 minute intervals. Playback at 10 frames per second (600X real time).

Video 3. Anaphase in RPE-1 cells.

Anaphase chromosome segregation in RPE-1 cells expressing KIF22-GFP (left), KIF22-GFP R149Q (middle), or KIF22-GFP V475G (right). Magenta: SiR-Tubulin, green: KIF22-GFP. Times indicate minutes after anaphase onset. Scale bar 5 μm. Cells were imaged at 1 minute intervals. Playback at 10 frames per second (600X real time).

Video 4. Anaphase spindle pole separation.

Anaphase in HeLa-Kyoto cells expressing pericentrin-RFP (magenta), CENPB-mCh (magenta), and KIF22-GFP (cyan). Times indicate seconds after anaphase onset. Scale bar 5 μm. Cells were imaged at 20 second intervals. Playback at 15 frames per second (300X real time).

Video 5. Cytokinesis and cytokinesis failure.

Mitosis and cytokinesis in HeLa-Kyoto cells expressing KIF22-GFP (left), KIF22-GFP R149Q (middle), or KIF22-GFP V475G (right) (all KIF22-GFP represented in green) and mCh-CAAX (magenta). Scale bar 10 μm. Cells were imaged at 3 minute intervals. Playback at 25 frames per second (4500X real time).

REFERENCES

Adzhubei, I. A., Schmidt, S., Peshkin, L., Ramensky, V. E., Gerasimova, A., Bork, P., et al. (2010). A method and server for predicting damaging missense mutations. *Nature Methods*, *7*(4), 248–249. http://doi.org/10.1038/nmeth0410-248

Antonio, C., Ferby, I., Wilhelm, H., Jones, M., Karsenti, E., Nebreda, A. R., & Vernos, I. (2000). Xkid, a chromokinesin required for chromosome alignment on the metaphase plate. *Cell*, *102*(4), 425–435. http://doi.org/10.1016/s0092-8674(00)00048-9

Asbury, C. L. (2017). Anaphase A: Disassembling Microtubules Move Chromosomes toward Spindle Poles. *Biology*, *6*(1), 15. http://doi.org/10.3390/biology6010015

Asselin, L., Alvarez, J. R., Heide, S., Bonnet, C. S., Tilly, P., Vitet, H., et al. (2020). Mutations in the KIF21B kinesin gene cause neurodevelopmental disorders through imbalanced canonical motor activity. *Nature Communications*, 1–18. http://doi.org/10.1038/s41467-020-16294-6

Bianchi, S., van Riel, W. E., Kraatz, S. H. W., Olieric, N., Frey, D., Katrukha, E. A., et al. (2016). Structural basis for misregulation of kinesin KIF21A autoinhibition by CFEOM1 disease mutations. *Scientific Reports*, *6*(1), 30668–16. http://doi.org/10.1038/srep30668

Bickel, K. G., Mann, B. J., Waitzman, J. S., Poor, T. A., Rice, S. E., & Wadsworth, P. (2017). Src family kinase phosphorylation of the motor domain of the human kinesin-5, Eg5. *Cytoskeleton (Hoboken, N.J.)*, *74*(9), 317–330. http://doi.org/10.1002/cm.21380

Bieling, P., Kronja, I., & Surrey, T. (2010). Microtubule Motility on Reconstituted Meiotic Chromatin. *Current Biology*, *20*(8), 763–769. http://doi.org/10.1016/j.cub.2010.02.067

Blasius, T. L., Yue, Y., Prasad, R., Liu, X., Gennerich, A., & Verhey, K. J. (2021). Sequences in the stalk domain regulate auto-inhibition and ciliary tip localization of the immotile kinesin-4 KIF7. *Journal of Cell Science*, *134*(13). http://doi.org/10.1242/jcs.258464

Bodnar, A. G., Ouellette, M., Frolkis, M., Holt, S. E., Chiu, C. P., Morin, G. B., et al. (1998). Extension of life-span by introduction of telomerase into normal human cells. *Science (New York, N.Y.)*, *279*(5349), 349–352. http://doi.org/10.1126/science.279.5349.349

Boyden, E. D., Campos-Xavier, A. B., Kalamajski, S., Cameron, T. L., Suarez, P., Tanackovic, G., et al. (2011). Recurrent dominant mutations affecting two adjacent residues in the motor domain of the monomeric kinesin KIF22 result in skeletal dysplasia and joint laxity. *American Journal of Human Genetics*, *89*(6), 767–772. http://doi.org/10.1016/j.ajhg.2011.10.016

Brouhard, G. J., & Hunt, A. J. (2005). Microtubule movements on the arms of mitotic chromosomes: polar ejection forces quantified in vitro. *Proceedings of the National Academy of Sciences*, *102*(39), 13903–13908. http://doi.org/10.1073/pnas.0506017102

1346 Brust-Mascher, I., Civelekoglu-Scholey, G., Kwon, M., Mogilner, A., & Scholey, J. M. (2004).
1347 Model for anaphase B: role of three mitotic motors in a switch from poleward flux to spindle
1348 elongation. *Proceedings of the National Academy of Sciences*, *101*(45), 15938–15943.
1349 http://doi.org/10.1073/pnas.0407044101
1350 Cameron, L. A., Yang, G., Cimini, D., Canman, J. C., Kisurina-Evgenieva, O., Khodjakov, A., et
1351 al. (2006). Kinesin 5-independent poleward flux of kinetochore microtubules in PtK1 cells.
1352 *The Journal of Cell Biology*, *173*(2), 173–179. http://doi.org/10.1083/jcb.200601075
1353 Cassimeris, L., Rieder, C. L., & Salmon, E. D. (1994). Microtubule Assembly and Kinetochore
1354 Directional Instability in Vertebrate Monopolar Spindles - Implications for the Mechanism of
1355 Chromosome Congression. *Journal of Cell Science*, *107*, 285–297.
1356 Cheng, L., Desai, J., Miranda, C. J., Duncan, J. S., Qiu, W., Nugent, A. A., et al. (2014). Human
1357 CFEOM1 Mutations Attenuate KIF21A Autoinhibition and Cause Oculomotor Axon Stalling.
1358 *Neuron*, *82*(2), 334–349. http://doi.org/10.1016/j.neuron.2014.02.038
1359 Chiba, K., Ori-McKenney, K. M., Niwa, S., & McKenney, R. J. (2021). Reconstitution of Kinesin-
1360 1 Activation. *Biorxiv.org*. http://doi.org/10.1101/2021.03.12.434960
1361 Choudhary, C., Kumar, C., Gnad, F., Nielsen, M. L., Rehman, M., Walther, T. C., et al. (2009).
1362 Lysine acetylation targets protein complexes and co-regulates major cellular functions.
1363 *Science (New York, N.Y.)*, *325*(5942), 834–840. http://doi.org/10.1126/science.1175371
1364 Cimini, D., Cameron, L. A., & Salmon, E. D. (2004). Anaphase spindle mechanics prevent mis-
1365 segregation of merotelically oriented chromosomes. *Current Biology*, *14*(23), 2149–2155.
1366 http://doi.org/10.1016/j.cub.2004.11.029
1367 Civelekoglu-Scholey, G., He, B., Shen, M., Wan, X., Roscioli, E., Bowden, B., & Cimini, D.
1368 (2013). Dynamic bonds and polar ejection force distribution explain kinetochore oscillations
1369 in PtK1 cells. *The Journal of Cell Biology*, *201*(4), 577–593.
1370 http://doi.org/10.1083/jcb.201301022
1371 Cousin, M. A., Conboy, E., Wang, J.-S., Lenz, D., Schwab, T. L., Williams, M., et al. (2019).
1372 RINT1 Bi-allelic Variations Cause Infantile-Onset Recurrent Acute Liver Failure and Skeletal
1373 Abnormalities. *American Journal of Human Genetics*, *105*(1), 108–121.
1374 http://doi.org/10.1016/j.ajhg.2019.05.011
1375 Coy, D. L., Hancock, W. O., Wagenbach, M., & Howard, J. (1999). Kinesin's tail domain is an
1376 inhibitory regulator of the motor domain. *Nature Cell Biology*, *1*(5), 288–292.
1377 http://doi.org/10.1038/13001
1378 Dephoure, N., Zhou, C., Villén, J., Beausoleil, S. A., Bakalarski, C. E., Elledge, S. J., & Gygi, S.
1379 P. (2008). A quantitative atlas of mitotic phosphorylation. *Proceedings of the National*
1380 *Academy of Sciences of the United States of America*, *105*(31), 10762–10767.
1381 http://doi.org/10.1073/pnas.0805139105
1382 Dodds, G. S. (1930). Row formation and other types of arrangement of cartilage cells in
1383 endochondral ossification. *The Anatomical Record*, *46*(4), 385–399.
1384 http://doi.org/10.1002/ar.1090460409
1385 Espeut, J., Gaussen, A., Bieling, P., Morin, V., Prieto, S., Fesquet, D., et al. (2008).
1386 Phosphorylation Relieves Autoinhibition of the Kinetochore Motor Cenp-E. *Molecular Cell*,
1387 *29*(5), 637–643. http://doi.org/10.1016/j.molcel.2008.01.004
1388 Friedman, D. S., & Vale, R. D. (1999). Single-molecule analysis of kinesin motility reveals
1389 regulation by the cargo-binding tail domain. *Nature Cell Biology*, *1*(5), 293–297.
1390 http://doi.org/10.1038/13008
1391 Fu, C., Ward, J. J., Loiodice, I., Velve-Casquillas, G., Nedelec, F. J., & Tran, P. T. (2009).
1392 Phospho-Regulated Interaction between Kinesin-6 Klp9p and Microtubule Bundler Ase1p
1393 Promotes Spindle Elongation. *Developmental Cell*, *17*(2), 257–267.
1394 http://doi.org/10.1016/j.devcel.2009.06.012

Funabiki, H., & Murray, A. W. (2000). The Xenopus chromokinesin Xkid is essential for metaphase chromosome alignment and must be degraded to allow anaphase chromosome movement. *Cell*, *102*(4), 411–424.

Gan, H., Xue, W., Gao, Y., Zhu, G., Chan, D., Cheah, K. S. E., & Huang, J. (2019). KIF5B modulates central spindle organization in late-stage cytokinesis in chondrocytes. *Cell & Bioscience*, 1–16. http://doi.org/10.1186/s13578-019-0344-5

Gillingham, A. K., & Munro, S. (2000). The PACT domain, a conserved centrosomal targeting motif in the coiled-coil proteins AKAP450 and pericentrin. *EMBO Reports*, *1*(6), 524–529. http://doi.org/10.1093/embo-reports/kvd105

Haila, S., Hästbacka, J., Böhling, T., Karjalainen-Lindsberg, M. L., Kere, J., & Saarialho-Kere, U. (2001). SLC26A2 (diastrophic dysplasia sulfate transporter) is expressed in developing and mature cartilage but also in other tissues and cell types. *The Journal of Histochemistry and Cytochemistry : Official Journal of the Histochemistry Society*, *49*(8), 973–982. http://doi.org/10.1177/002215540104900805

Hammond, J. W., Blasius, T. L., Soppina, V., Cai, D., & Verhey, K. J. (2010). Autoinhibition of the kinesin-2 motor KIF17 via dual intramolecular mechanisms. *The Journal of Cell Biology*, *189*(6), 1013–1025. http://doi.org/10.1083/jcb.201001057

Hammond, J. W., Cai, D., Blasius, T. L., Li, Z., Jiang, Y., Jih, G. T., et al. (2009). Mammalian Kinesin-3 Motors Are Dimeric In Vivo and Move by Processive Motility upon Release of Autoinhibition. *PLOS Biology*, *7*(3), e1000072–14. http://doi.org/10.1371/journal.pbio.1000072

Hatch, E. M., Fischer, A. H., Deerinck, T. J., & Hetzer, M. W. (2013). Catastrophic Nuclear Envelope Collapse in Cancer Cell Micronuclei. *Cell*, *154*(1), 47–60. http://doi.org/10.1016/j.cell.2013.06.007

Hegemann, B., Hutchins, J. R. A., Hudecz, O., Novatchkova, M., Rameseder, J., Sykora, M. M., et al. (2011). Systematic phosphorylation analysis of human mitotic protein complexes. *Science Signaling*, *4*(198), rs12. http://doi.org/10.1126/scisignal.2001993

Hershko, A. (1999). Mechanisms and regulation of the degradation of cyclin B. *Philosophical Transactions of the Royal Society of London. Series B, Biological Sciences*, *354*(1389), 1571–5– discussion 1575–6. http://doi.org/10.1098/rstb.1999.0500

Iemura, K., & Tanaka, K. (2015). Chromokinesin Kid and kinetochore kinesin CENP-E differentially support chromosome congression without end-on attachment to microtubules. *Nature Communications*, *6*, 1–11. http://doi.org/10.1038/ncomms7447

Imanishi, M., Endres, N. F., Gennerich, A., & Vale, R. D. (2006). Autoinhibition regulates the motility of the C. elegans intraflagellar transport motor OSM-3. *The Journal of Cell Biology*, *174*(7), 931–937. http://doi.org/10.1083/jcb.200605179

Ioannidis, N. M., Rothstein, J. H., Pejaver, V., Middha, S., McDonnell, S. K., Baheti, S., et al. (2016). REVEL: An Ensemble Method for Predicting the Pathogenicity of Rare Missense Variants. *The American Journal of Human Genetics*, *99*(4), 877–885. http://doi.org/10.1016/j.ajhg.2016.08.016

Kettenbach, A. N., Schweppe, D. K., Faherty, B. K., Pechenick, D., Pletnev, A. A., & Gerber, S. A. (2011). Quantitative phosphoproteomics identifies substrates and functional modules of Aurora and Polo-like kinase activities in mitotic cells. *Science Signaling*, *4*(179), rs5. http://doi.org/10.1126/scisignal.2001497

Khandelia, P., Yap, K., & Makeyev, E. V. (2011). Streamlined platform for short hairpin RNA interference and transgenesis in cultured mammalian cells. *Proceedings of the National Academy of Sciences of the United States of America*, *108*(31), 12799–12804. http://doi.org/10.1073/pnas.1103532108

Lefeber, D. J., Morava, E., & Jaeken, J. (2011). How to find and diagnose a CDG due to defective N-glycosylation. *Journal of Inherited Metabolic Disease*, *34*(4), 849–852. http://doi.org/10.1007/s10545-011-9370-0

1446 Levesque, A. A., & Compton, D. A. (2001). The chromokinesin Kid is necessary for
1447 chromosome arm orientation and oscillation, but not congression, on mitotic spindles. *The*
1448 *Journal of Cell Biology*, *154*(6), 1135–1146. http://doi.org/10.1083/jcb.200106093
1449 Levesque, A. A., Howard, L., Gordon, M. B., & Compton, D. A. (2003). A functional relationship
1450 between NuMA and kid is involved in both spindle organization and chromosome alignment
1451 in vertebrate cells. *Molecular Biology of the Cell*, *14*(9), 3541–3552.
1452 http://doi.org/10.1091/mbc.E03-02-0082
1453 Liu, D., Vleugel, M., Backer, C. B., Hori, T., Fukagawa, T., Cheeseman, I. M., & Lampson, M. A.
1454 (2010). Regulated targeting of protein phosphatase 1 to the outer kinetochore by KNL1
1455 opposes Aurora B kinase. *The Journal of Cell Biology*, *188*(6), 809–820.
1456 http://doi.org/10.1083/jcb.201001006
1457 Liu, Y., Mi, Y., Mueller, T., Kreibich, S., Williams, E. G., Van Drogen, A., et al. (2018). Genomic,
1458 Proteomic and Phenotypic Heterogeneity in HeLa Cells across Laboratories: Implications
1459 for Reproducibility of Research Results. *bioRxiv*, 307421. http://doi.org/10.1101/307421
1460 Marquis, C., Fonseca, C. L., Queen, K. A., Wood, L., Vandal, S. E., Malaby, H. L. H., et al.
1461 (2021). Chromosomally unstable tumor cells specifically require KIF18A for proliferation.
1462 *Nature Communications*, 1–14. http://doi.org/10.1038/s41467-021-21447-2
1463 Marshall, W. F., Marko, J. F., Agard, D. A., & Sedat, J. W. (2001). Chromosome elasticity and
1464 mitotic polar ejection force measured in living Drosophila embryos by four-dimensional
1465 microscopy-based motion analysis. *Current Biology*, *11*(8), 569–578.
1466 http://doi.org/10.1016/s0960-9822(01)00180-4
1467 Min, B.-J., Kim, N., Chung, T., Kim, O.-H., Nishimura, G., Chung, C. Y., et al. (2011). Whole-
1468 exome sequencing identifies mutations of KIF22 in spondyloepimetaphyseal dysplasia with
1469 joint laxity, leptodactylic type. *American Journal of Human Genetics*, *89*(6), 760–766.
1470 http://doi.org/10.1016/j.ajhg.2011.10.015
1471 Morgan, D. O. (1995). Principles of CDK regulation. *Nature*, *374*(6518), 131–134.
1472 http://doi.org/10.1038/374131a0
1473 Muretta, J. M., Reddy, B. J. N., Scarabelli, G., Thompson, A. F., Jariwala, S., Major, J., et al.
1474 (2018). A posttranslational modification of the mitotic kinesin Eg5 that enhances its
1475 mechanochemical coupling and alters its mitotic function. *Proceedings of the National*
1476 *Academy of Sciences*, *74*, 201718290–10. http://doi.org/10.1073/pnas.1718290115
1477 Nislow, C., Lombillo, V. A., Kuriyama, R., & McIntosh, J. R. (1992). A plus-end-directed motor
1478 enzyme that moves antiparallel microtubules in vitro localizes to the interzone of mitotic
1479 spindles. *Nature*, *359*(6395), 543–547. http://doi.org/10.1038/359543a0
1480 Ohsugi, M., Adachi, K., Horai, R., Kakuta, S., Sudo, K., Kotaki, H., et al. (2008). Kid-Mediated
1481 Chromosome Compaction Ensures Proper Nuclear Envelope Formation. *Cell*, *132*(5), 771–
1482 782. http://doi.org/10.1016/j.cell.2008.01.029
1483 Ohsugi, M., Tokai-Nishizumi, N., Shiroguchi, K., Toyoshima, Y. Y., Inoue, J.-I., & Yamamoto, T.
1484 (2003). Cdc2-mediated phosphorylation of Kid controls its distribution to spindle and
1485 chromosomes. *The EMBO Journal*, *22*(9), 2091–2103. http://doi.org/10.1093/emboj/cdg208
1486 Olsen, J. V., Vermeulen, M., Santamaria, A., Kumar, C., Miller, M. L., Jensen, L. J., et al.
1487 (2010). Quantitative phosphoproteomics reveals widespread full phosphorylation site
1488 occupancy during mitosis. *Science Signaling*, *3*(104), ra3.
1489 http://doi.org/10.1126/scisignal.2000475
1490 Pant, D., Parameswaran, J., Rao, L., Shi, L., Chilukuri, G., McEachin, Z. T., et al. (2022). ALS-
1491 linked KIF5A ΔExon27 mutant causes neuronal toxicity through gain of function. *Biorxiv.org*
1492 . http://doi.org/10.1101/2022.03.05.483071
1493 Quang, D., Chen, Y., & Xie, X. (2015). DANN: a deep learning approach for annotating the
1494 pathogenicity of genetic variants. *Bioinformatics (Oxford, England)*, *31*(5), 761–763.
1495 http://doi.org/10.1093/bioinformatics/btu703

1496 Ren, J., Wang, S., Chen, H., Wang, W., Huo, L., & Feng, W. (2018). Coiled-coil 1-mediated
1497 fastening of the neck and motor domains for kinesin-3 autoinhibition. *Proceedings of the*
1498 *National Academy of Sciences of the United States of America*, *115*(51), E11933–E11942.
1499 http://doi.org/10.1073/pnas.1811209115
1500 Rentzsch, P., Witten, D., Cooper, G. M., Shendure, J., & Kircher, M. (2018). CADD: predicting
1501 the deleteriousness of variants throughout the human genome, 1–9.
1502 http://doi.org/10.1093/nar/gky1016
1503 Rieder, C. L., & Salmon, E. D. (1994). Motile kinetochores and polar ejection forces dictate
1504 chromosome position on the vertebrate mitotic spindle. *The Journal of Cell Biology*, *124*(3),
1505 223–233. http://doi.org/10.1083/jcb.124.3.223
1506 Rieder, C. L., Davison, E. A., Jensen, L. C., Cassimeris, L., & Salmon, E. D. (1986). Oscillatory
1507 movements of monooriented chromosomes and their position relative to the spindle pole
1508 result from the ejection properties of the aster and half-spindle. *The Journal of Cell Biology*,
1509 *103*(2), 581–591. http://doi.org/10.1083/jcb.103.2.581
1510 Rigbolt, K. T. G., Prokhorova, T. A., Akimov, V., Henningsen, J., Johansen, P. T.,
1511 Kratchmarova, I., et al. (2011). System-wide temporal characterization of the proteome and
1512 phosphoproteome of human embryonic stem cell differentiation. *Science Signaling*, *4*(164),
1513 rs3. http://doi.org/10.1126/scisignal.2001570
1514 Ris, H. (1949). The anaphase movement of chromosomes in the spermatocytes of the
1515 grasshopper. *The Biological Bulletin*, *96*(1), 90–106.
1516 Rossi, A., & Superti-Furga, A. (2001). Mutations in the diastrophic dysplasia sulfate transporter
1517 (DTDST) gene (SLC26A2): 22 novel mutations, mutation review, associated skeletal
1518 phenotypes, and diagnostic relevance. *Human Mutation*, *17*(3), 159–171.
1519 http://doi.org/10.1002/humu.1
1520 Samwer, M., Schneider, M. W. G., Hoefler, R., Schmalhorst, P. S., Jude, J. G., Zuber, J., &
1521 Gerlich, D. W. (2017). DNA Cross-Bridging Shapes a Single Nucleus from a Set of Mitotic
1522 Chromosomes. *Cell*, *170*(5), 956–972.e23. http://doi.org/10.1016/j.cell.2017.07.038
1523 Sawin, K. E., LeGuellec, K., Philippe, M., & Mitchison, T. J. (1992). Mitotic spindle organization
1524 by a plus-end-directed microtubule motor. *Nature*, *359*(6395), 540–543.
1525 http://doi.org/10.1038/359540a0
1526 Schindelin, J., Arganda-Carreras, I., Frise, E., Kaynig, V., Longair, M., Pietzsch, T., et al. (2012).
1527 Fiji: an open-source platform for biological-image analysis. *Nature Methods*, *9*(7), 676–682.
1528 http://doi.org/10.1038/nmeth.2019
1529 Schneider, C. A., Rasband, W. S., & Eliceiri, K. W. (2012). NIH Image to ImageJ: 25 years of
1530 image analysis. *Nature Methods*, 1–5. http://doi.org/10.1038/nmeth.2089
1531 Schwarz, J. M., Rödelsperger, C., Schuelke, M., & Seelow, D. (2010). MutationTaster evaluates
1532 disease-causing potential of sequence alterations. *Nature Publishing Group*, 1–2.
1533 http://doi.org/10.1038/nmeth0810-575
1534 Serra-Marques, A., Houtekamer, R., Hintzen, D., Canty, J. T., Yildiz, A., & Dumont, S. (2020).
1535 The mitotic protein NuMA plays a spindle-independent role in nuclear formation and
1536 mechanics. *The Journal of Cell Biology*, *219*(12), 348–23.
1537 http://doi.org/10.1083/jcb.202004202
1538 Sharma, K., D'Souza, R. C. J., Tyanova, S., Schaab, C., Wisniewski, J. R., Cox, J., & Mann, M.
1539 (2014). Ultradeep Human Phosphoproteome Reveals a Distinct Regulatory Nature of Tyr
1540 and Ser/Thr-Based Signaling. *Cell Reports*, *8*(5), 1583–1594.
1541 http://doi.org/10.1016/j.celrep.2014.07.036
1542 Shiroguchi, K., Ohsugi, M., Edamatsu, M., Yamamoto, T., & Toyoshima, Y. Y. (2003). The
1543 Second Microtubule-binding Site of Monomeric Kid Enhances the Microtubule Affinity. *The*
1544 *Journal of Biological Chemistry*, *278*(25), 22460–22465.
1545 http://doi.org/10.1074/jbc.M212274200

Shiromizu, T., Adachi, J., Watanabe, S., Murakami, T., Kuga, T., Muraoka, S., & Tomonaga, T. (2013). Identification of missing proteins in the neXtProt database and unregistered phosphopeptides in the PhosphoSitePlus database as part of the Chromosome-centric Human Proteome Project. *Journal of Proteome Research*, *12*(6), 2414–2421. http://doi.org/10.1021/pr300825v

Soeda, S., Yamada-Nomoto, K., & Ohsugi, M. (2016). The microtubule-binding and coiled-coil domains of Kid are required to turn off the polar ejection force at anaphase. *Journal of Cell Science*, *129*(19), 3609–3619. http://doi.org/10.1242/jcs.189969

Straight, A. F., Sedat, J. W., & Murray, A. W. (1998). Time-lapse microscopy reveals unique roles for kinesins during anaphase in budding yeast. *The Journal of Cell Biology*, *143*(3), 687–694. http://doi.org/10.1083/jcb.143.3.687

Stumpff, J., Dassow, von, G., Wagenbach, M., Asbury, C., & Wordeman, L. (2008). The Kinesin-8 Motor Kif18A Suppresses Kinetochore Movements to Control Mitotic Chromosome Alignment. *Developmental Cell*, *14*(2), 252–262. http://doi.org/10.1016/j.devcel.2007.11.014

Stumpff, J., Wagenbach, M., Franck, A., Asbury, C. L., & Wordeman, L. (2012). Kif18A and Chromokinesins Confine Centromere Movements via Microtubule Growth Suppression and Spatial Control of Kinetochore Tension. *Developmental Cell*, *22*(5), 1017–1029. http://doi.org/10.1016/j.devcel.2012.02.013

Sturgill, E. G., Norris, S. R., Guo, Y., & Ohi, R. (2016). Kinesin-5 inhibitor resistance is driven by kinesin-12. *The Journal of Cell Biology*, *213*(2), 213–227. http://doi.org/10.1083/jcb.201507036

Su, K.-C., Barry, Z., Schweizer, N., Maiato, H., Bathe, M., & Cheeseman, I. M. (2016). A Regulatory Switch Alters Chromosome Motions at the Metaphase-to-Anaphase Transition. *Cell Reports*, *17*(7), 1728–1738. http://doi.org/10.1016/j.celrep.2016.10.046

Takagi, J., Itabashi, T., Suzuki, K., & Ishiwata, S. (2013). Chromosome position at the spindle equator is regulated by chromokinesin and a bipolar microtubule array. *Scientific Reports*, *3*, 746–7. http://doi.org/10.1038/srep02808

Tanenbaum, M. E., Macůrek, L., Janssen, A., Geers, E. F., Alvarez-Fernández, M., & Medema, R. H. (2009). Kif15 Cooperates with Eg5 to Promote Bipolar Spindle Assembly. *Current Biology*, *19*(20), 1703–1711. http://doi.org/10.1016/j.cub.2009.08.027

Thompson, A. F., Vandal, S., & Stumpff, J. (2022). Quantifying Changes in Chromosome Position to Assess Chromokinesin Activity. *Methods in Molecular Biology (Clifton, N.J.)*, *2415*, 139–149. http://doi.org/10.1007/978-1-0716-1904-9_10

Tokai, N., Fujimoto-Nishiyama, A., Toyoshima, Y., Yonemura, S., Tsukita, S., Inoue, J., & Yamamoto, T. (1996). Kid, a novel kinesin-like DNA binding protein, is localized to chromosomes and the mitotic spindle. *The EMBO Journal*, *15*(3), 457–467.

Tokai-Nishizumi, N., Ohsugi, M., Suzuki, E., & Yamamoto, T. (2005). The chromokinesin kid is required for maintenance of proper metaphase spindle size. *Molecular Biology of the Cell*, *16*(11), 5455–5463. http://doi.org/10.1091/mbc.E05-03-0244

Tüysüz, B., Yılmaz, S., Erener-Ercan, T., Bilguvar, K., & Günel, M. (2014). Spondyloepimetaphyseal dysplasia with joint laxity, leptodactylic type: longitudinal observation of radiographic findings in a child heterozygous for a KIF22 mutation. *Pediatric Radiology*, *45*(5), 771–776. http://doi.org/10.1007/s00247-014-3159-x

Uhlen, M., Fagerberg, L., Hallström, B. M., Lindskog, C., Oksvold, P., Mardinoglu, A., et al. (2015). Tissue-based map of the human proteome. *Science (New York, N.Y.)*, *347*(6220), 1260419–1260419. http://doi.org/10.1126/science.1260419

van der Vaart, B., van Riel, W. E., Doodhi, H., Kevenaar, J. T., Katrukha, E. A., Gumy, L., et al. (2013). CFEOM1-Associated Kinesin KIF21A Is a Cortical Microtubule Growth Inhibitor. *Developmental Cell*, *27*(2), 145–160. http://doi.org/10.1016/j.devcel.2013.09.010

van Heesbeen, R. G. H. P., Tanenbaum, M. E., & Medema, R. H. (2014). Balanced Activity of Three Mitotic Motors Is Required for Bipolar Spindle Assembly and Chromosome Segregation. *Cell Reports*, *8*(4), 948–956. http://doi.org/10.1016/j.celrep.2014.07.015

Vaser, R., Adusumalli, S., Leng, S. N., Sikic, M., & Ng, P. C. (2015). SIFT missense predictions for genomes. *Nature Protocols*, *11*(1), 1–9. http://doi.org/10.1038/nprot.2015-123

Verhey, K. J., & Hammond, J. W. (2009). Cytoskeletal motors: Traffic control: regulation of kinesin motors, 1–13. http://doi.org/10.1038/nrm2782

Verhey, K. J., Lizotte, D. L., Abramson, T., Barenboim, L., Schnapp, B. J., & Rapoport, T. A. (1998). Light chain-dependent regulation of Kinesin's interaction with microtubules. *The Journal of Cell Biology*, *143*(4), 1053–1066. http://doi.org/10.1083/jcb.143.4.1053

Vukušić, K., Buđa, R., & Tolić, I. M. (2019). Force-generating mechanisms of anaphase in human cells. *Journal of Cell Science*, *132*(18), jcs231985–11. http://doi.org/10.1242/jcs.231985

Vukušić, K., Ponjavić, I., Buđa, R., Risteski, P., & Tolić, I. M. (2021). Microtubule-sliding modules based on kinesins EG5 and PRC1-dependent KIF4A drive human spindle elongation. *Developmental Cell*, 1–42. http://doi.org/10.1016/j.devcel.2021.04.005

Wandke, C., Barisic, M., Sigl, R., Rauch, V., Wolf, F., Amaro, A. C., et al. (2012). Human chromokinesins promote chromosome congression and spindle microtubule dynamics during mitosis. *The Journal of Cell Biology*, *198*(5), 847–863. http://doi.org/10.1083/jcb.201110060

Wolf, F., Wandke, C., Isenberg, N., & Geley, S. (2006). Dose-dependent effects of stable cyclin B1 on progression through mitosis in human cells. *The EMBO Journal*, *25*(12), 2802–2813. http://doi.org/10.1038/sj.emboj.7601163

Yajima, J., Edamatsu, M., Watai-Nishii, J., Tokai-Nishizumi, N., Yamamoto, T., & Toyoshima, Y. Y. (2003). The human chromokinesin Kid is a plus end-directed microtubule-based motor. *The EMBO Journal*, *22*(5), 1067–1074. http://doi.org/10.1093/emboj/cdg102

Zhang, P., Knowles, B. A., Goldstein, L. S., & Hawley, R. S. (1990). A kinesin-like protein required for distributive chromosome segregation in Drosophila. *Cell*, *62*(6), 1053–1062.